Stretch-activated ion channel TMEM63B associates with developmental and epileptic encephalopathies and progressive neurodegeneration

Graphical abstract

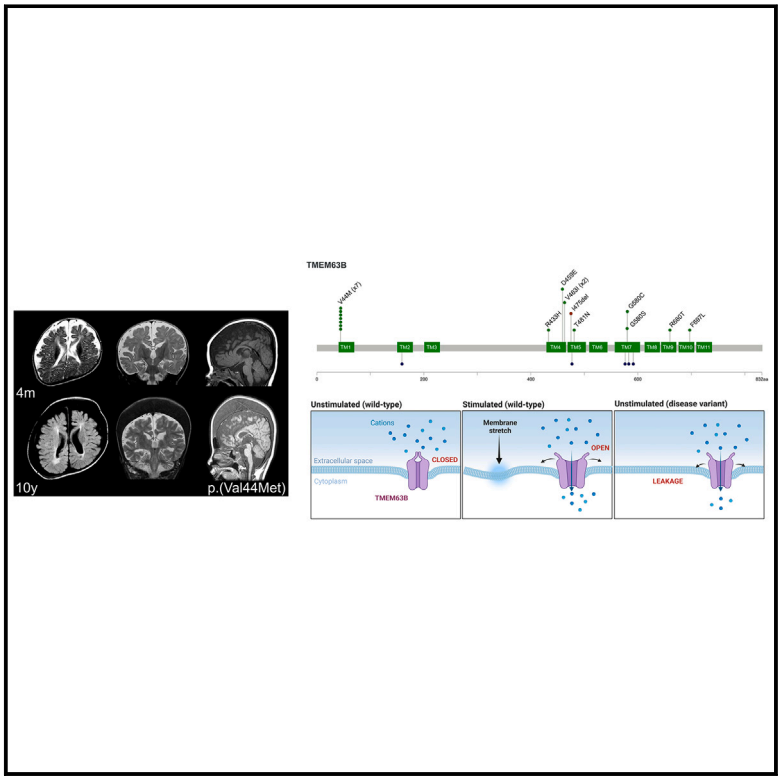

Authors

Annalisa Vetro, Cristiana Pelorosso, Simona Balestrini, ..., Naomichi Matsumoto, Gian Michele Ratto, Renzo Guerrini

Correspondence

r.guerrini@meyer.it

Combining *in silico* evaluation, *in vitro* electrophysiology and Ca^{2+} imaging, and *in vivo* modeling in *Drosophila*, Vetro et al. demonstrate that gain-of-function variants of the stretch-activated ion channel TMEM63B cause a severe neurodevelopmental disorder with early-onset epilepsy and progressive brain damage associated with hematological abnormalities in most individuals.

Vetro et al., 2023, The American Journal of Human Genetics *110*, 1356–1376
August 3, 2023

https://doi.org/10.1016/j.ajhg.2023.06.008

ARTICLE

Stretch-activated ion channel TMEM63B associates with developmental and epileptic encephalopathies and progressive neurodegeneration

Annalisa Vetro,[1,38] Cristiana Pelorosso,[1,38] Simona Balestrini,[1,2,38] Alessio Masi,[3] Sophie Hambleton,[4,5] Emanuela Argilli,[6] Valerio Conti,[1] Simone Giubbolini,[7] Rebekah Barrick,[8] Gaber Bergant,[9] Karin Writzl,[9] Emilia K. Bijlsma,[10] Theresa Brunet,[11,12] Pilar Cacheiro,[13] Davide Mei,[1] Anita Devlin,[4,5] Mariëtte J.V. Hoffer,[10] Keren Machol,[14] Guido Mannaioni,[3] Masamune Sakamoto,[15] Manoj P. Menezes,[16] Thomas Courtin,[17,18] Elliott Sherr,[6] Riccardo Parra,[7] Ruth Richardson,[19] Tony Roscioli,[20,21] Marcello Scala,[22] Celina von Stülpnagel,[12,23] Damian Smedley,[13] TMEM63B collaborators, The Genomics England Research Consortium, Annalaura Torella,[24,25] Jun Tohyama,[26] Reiko Koichihara,[27] Keisuke Hamada,[28] Kazuhiro Ogata,[28] Takashi Suzuki,[29] Atsushi Sugie,[30] Jasper J. van der Smagt,[31] Koen van Gassen,[31] Stephanie Valence,[32,33] Emma Vittery,[19] Stephen Malone,[34,35] Mitsuhiro Kato,[36] Naomichi Matsumoto,[15] Gian Michele Ratto,[7,37] and Renzo Guerrini[1,2,*]

Summary

By converting physical forces into electrical signals or triggering intracellular cascades, stretch-activated ion channels allow the cell to respond to osmotic and mechanical stress. Knowledge of the pathophysiological mechanisms underlying associations of stretch-activated ion channels with human disease is limited. Here, we describe 17 unrelated individuals with severe early-onset developmental and epileptic encephalopathy (DEE), intellectual disability, and severe motor and cortical visual impairment associated with progressive neurodegenerative brain changes carrying ten distinct heterozygous variants of *TMEM63B*, encoding for a highly conserved stretch-activated ion channel. The variants occurred *de novo* in 16/17 individuals for whom parental DNA was available and either missense, including the recurrent p.Val44Met in 7/17 individuals, or in-frame, all affecting conserved residues located in transmembrane regions of the protein. In 12 individuals, hematological abnormalities co-occurred, such as macrocytosis and hemolysis, requiring blood transfusions in some. We modeled six variants (p.Val44Met, p.Arg433His, p.Thr481Asn, p.Gly580Ser, p.Arg660Thr, and p.Phe697Leu), each affecting a distinct transmembrane domain of the channel, in transfected Neuro2a cells and demonstrated inward leak cation currents across the mutated channel even in isotonic conditions, while the response to hypo-osmotic challenge was impaired, as were the Ca^{2+} transients generated under hypo-osmotic stimulation. Ectopic expression of the p.Val44Met and p.Gly580Cys variants in *Drosophila* resulted in early death. *TMEM63B*-associated DEE represents a recognizable clinicopathological entity in which altered cation conductivity results in a severe neurological phenotype with progressive brain damage and early-onset epilepsy associated with hematological abnormalities in most individuals.

[1]Neuroscience Department, Meyer Children's Hospital IRCCS, Florence, Italy; [2]University of Florence, Florence, Italy; [3]Department of Neuroscience, Psychology, Drug Research and Child Health (NeuroFarBa), Section of Pharmacology and Toxicology, University of Florence, Florence, Italy; [4]Newcastle University Translational and Clinical Research Institute, Newcastle upon Tyne, UK; [5]Great North Children's Hospital, Newcastle upon Tyne Hospitals NHS Foundation Trust, Newcastle upon Tyne, UK; [6]Department of Neurology and Institute of Human Genetics and Weill Institute for Neurosciences, University of California, San Francisco, San Francisco, CA, USA; [7]National Enterprise for NanoScience and NanoTechnology (NEST), Istituto Nanoscienze, Consiglio Nazionale delle Ricerche (CNR) and Scuola Normale Superiore Pisa, Pisa, Italy; [8]Division of Metabolic Disorders, Children's Hospital of Orange County (CHOC), Orange, CA, USA; [9]Clinical Institute of Genomic Medicine, University Medical Centre Ljubljana, Ljubljana, Slovenia; [10]Department of Clinical Genetics, Leiden University Medical Center, Leiden, the Netherlands; [11]Institute of Human Genetics, School of Medicine, Technical University Munich, Munich, Germany; [12]Department of Pediatric Neurology and Developmental Medicine, Dr. v. Hauner Children's Hospital, LMU - University of Munich, München, Germany; [13]William Harvey Research Institute, Queen Mary University of London, London, UK; [14]Department of Molecular and Human Genetics, Baylor College of Medicine, Houston, TX 77030, USA; [15]Department of Human Genetics, Yokohama City University Graduate School of Medicine, Yokohama 236-0004 Japan; [16]Department of Neurology, The Children's Hospital at Westmead and the Children's Hospital at Westmead Clinical School, University of Sydney, Westmead NSW, Australia; [17]Sorbonne Université, Institut du Cerveau - Paris Brain Institute - ICM, Inserm, CNRS, Paris, France; [18]Assistance Publique Hôpitaux de Paris, Hôpital Pitié-Salpêtrière, Département de Génétique, DMU BioGeM, Paris, France; [19]Northern Genetics Service, Newcastle upon Tyne hospitals NHS Foundation Trust, Newcastle, UK; [20]New South Wales Health Pathology Randwick Genomics, Prince of Wales Hospital, Sydney, NSW 2031, Australia; [21]Neuroscience Research Australia, Sydney, NSW 2031, Australia; [22]Department of Neurosciences, Rehabilitation, Ophthalmology, Genetics, Maternal and Child Health, University of Genoa, Genoa, Italy; [23]Institute for Transition, Rehabilitation and Palliation, Paracelsus Medical University, Salzburg, Austria; [24]Department of Precision Medicine, University "Luigi Vanvitelli," Naples, Italy; [25]Telethon Institute of Genetics and Medicine (TIGEM), Pozzuoli, Italy; [26]Department of Child Neurology, Nishi-Niigata Chuo National Hospital, Niigata 950-2085, Japan; [27]Department for Child Health and Human Development, Saitama Children's Medical Center, Saitama 330-8777, Japan; [28]Department of Biochemistry, Yokohama City University Graduate School of Medicine, Yokohama 236-0004, Japan; [29]School of Life Science and Technology, Tokyo Institute of Technology, Yokohama, Kanagawa, Japan; [30]Brain Research Institute, Niigata University, Niigata 951-8585, Japan; [31]Department of Genetics, University Medical Center Utrecht, Utrecht, the Netherlands; [32]Centre de référence Maladies Rares "Déficience intellectuelle de cause rare," Sorbonne Université, Paris, France; [33]Département de Neuropédiatrie, Hôpital Armand Trousseau, APHP, Sorbonne Université, Paris, France; [34]Department of Neurosciences, Queensland Children's Hospital, Brisbane QLD, Australia; [35]Centre for Advanced Imaging, University of Queensland, St Lucia QLD, Australia; [36]Department of Pediatrics, Showa University School of Medicine, Tokyo 142-8666, Japan; [37]Istituto Neuroscienze CNR, Padova, Italy
[38]These authors contributed equally
*Correspondence: r.guerrini@meyer.it
https://doi.org/10.1016/j.ajhg.2023.06.008.

Introduction

TMEM63B, with its two paralogs *TMEM63A* and *C*, belongs to a gene family initially identified as the closest homologs of the OSCA proteins, which represent the largest family of stretch-activated ion channels conserved across eukaryotes.[1,2] In plants, members of the OSCA family sense osmotic stress-induced mechanical forces across the plasma membrane and activate a signaling pathway responsible for regulating water transpiration and root growth.[1,3] In mammals, members of the TMEM63 family mediate cation currents in response to osmotic and mechanical stimuli affecting membrane tension.[1,4] This process is crucial for cell volume regulation and viability, as changes in osmolarity may cause water influx or efflux through the plasma membrane, resulting in cell swelling or shrinkage.[5]

Other members of the *TMEM63* family have been associated with monogenic disorders, namely transient infantile hypomyelinating leukodystrophy-19 (HLD19 [MIM: 618688]), with developmental delay of variable severity caused by heterozygous *TMEM63A* variants,[6–8] and autosomal recessive spastic paraplegia-87 (SPC-87 [MIM: 619966]), caused by biallelic truncating variants of *TMEM63C*.[9] The *TMEM63B* gene still lacks a clear association with human diseases and is not yet listed either in the OMIM's Morbid Map of the Human Genome or in the ClinGen Gene-Disease Validity database (https://www.clinicalgenome.org/). The gene is ubiquitously expressed in humans, and, according to the GTEx portal (https://www.gtexportal.org/home/), multiple *TMEM63B* mRNA isoforms occur with different tissue specificity. Multiple *Tmem63b* mRNA isoforms have also been identified in mice, with post-transcriptional modifications contributing to mRNA diversity.[10] A brain-specific *Tmem63b* isoform, exhibiting alternative splicing of exon 4 and glutamine to arginine change (Q/R) at exon 20, has been shown to regulate Ca^{2+} permeability and osmosensitivity of the channel.[10]

We identified ten distinct heterozygous *de novo* variants of *TMEM63B* in 17 unrelated individuals with early-onset developmental and epileptic encephalopathy (DEE), all associated with white matter disease, corpus callosum abnormalities, and variable cortical, cerebellar, and hematological abnormalities.

After determining the most represented brain *TMEM63B* isoform in humans, we tested *in vitro* the effect of selected variants on the protein localization and function by immunocytochemistry, whole-cell patch clamp, and calcium imaging in transfected Neuro2a cells. We also modeled *in vivo* in *Drosophila* the effects of the ectopic expression of two variants. Our findings indicate that heterozygous variants of *TMEM63B* result in a clinically recognizable DEE syndrome whose pathophysiology lies in altered functional properties of the channel.

Material and methods

Research cohort

Our initial discovery cohort consisted of 600 consecutive individuals referred to the Neuroscience Department of the Meyer Children's Hospital to investigate the genetic causes of DEEs. Within this cohort, we identified by whole-exome sequencing (WES)[11] *de novo* heterozygous variants of *TMEM63B* in three individuals (IDs 1–3) with a homogeneous clinical and neuroimaging phenotype and promoted an international collaboration through GeneMatcher[12] identifying 14 additional individuals carrying *de novo TMEM63B* variants (IDs 4–17). We reviewed medical records, electroencephalograms (EEGs), and brain magnetic resonance imaging (MRI) scans. We classified seizure types following the International League Against Epilepsy (ILAE) criteria[13] whenever applicable and used more descriptive terms when seizure phenomenology could not fit classification terminology. We obtained written informed consent for the study from all participants or their legal guardians, according to local requirements. The study was approved by the Pediatric Ethics Committees of the Tuscany Region, Italy, in the context of the DESIRE FP7 EU project and its extension by the DECODE-EE project.

Detailed methods for MRI investigations, genetic and structural protein analyses, functional characterization of *TMEM63B* variants, and *Drosophila* modeling are reported in the supplemental information.

Results

Clinical findings

Clinical, EEG, and MRI findings of the 17 individuals are summarized in Tables 1 and S2. They were all unrelated subjects who exhibited a markedly overlapping DEE phenotype with early-onset drug-resistant epilepsy (17/17, 100%), severe developmental delay (17/17, 100%), early generalized hypotonia evolving to spastic quadriparesis (13/17, 76%), nystagmus and central visual impairment (11/17, 65%). Epilepsy onset ranged from birth to 3 years but occurred within the first year in 14/17 (82%) and in the first month of life in 6/17 (35%). A common pattern of the epilepsy phenotype was early onset of focal seizures (11/17, 65%), often manifested as apnoeic episodes in newborns, followed over months by epileptic spasms (5/17, 29%) or by different types of focal and generalized onset seizures (7/17, 41%). Infantile epileptic spasms, which were the initial manifestation of epilepsy in three additional individuals (3/17, 18%), had therefore been present in 9/17 individuals (53%). In two remaining individuals (2/17, 12%), onset was at 2 and 3 years with focal seizures with impaired awareness. Epilepsy was severe at onset in all individuals, with episodes of status epilepticus in three (3/17, 18%). At last follow-up, five individuals (5/17, 29%) no longer had severe epilepsy, including three who had experienced prolonged seizure freedom on medication (3/17, 18%).

EEGs showed slow background activity with bilateral independent or multifocal epileptiform discharges in most individuals.

Table 1. Clinical features of the 17 individuals with *TMEM63B* variants

Individuals' ID/gender	TMEM63B variant[a] (cDNA and protein)	Age at last follow-up/ death	Age at seizure onset/type	Seizure types/ severity during follow-up	Treatment ever tried (+ efficacy, +/− transient efficacy, − worsening or not tolerated)	EEG	Brain magnetic resonance imaging	Clinical neurological phenotype	Hematological findings
1/M	c.130G>A (p.Val44Met)	8 years/ deceased at 9 years (pneumonia)	6 months/ infantile spasms	spasms, myoclonic, focal with impaired awareness/daily	CZP, ESM, PB, VGB	6 months–8 years: slow background, bilateral independent discharges; epileptic spasms and myoclonic szs	5 months, 4 years: thin CC, colpocephaly, abnormal myelination, dysmorphic lateral ventricles, enlarged extracerebral spaces, progressive mild cerebellar atrophy, and watershed areas WM abnormality	threatened preterm labor at 35 weeks, global profound DD, generalized hypotonia, plagiocephaly, nystagmus, dysphagia (PEG 17 months), dyskinesias	mild anemia
2/M	c.1298G>A (p.Arg433His)	10 years	birth/focal	bilateral independent focal motor with impaired awareness, focal to bilateral tonic-clonic/weekly	CBZ, CLB, CZP, LEV, LCM, MDZ, PB, PHT, STP, TPM	7−10 years: slow background, multifocal discharges; focal szs recorded	6 years, 10 years: thin CC, multifocal WM abnormalities, ventricular asymmetry, progressive cerebellar atrophy	global profound DD, ataxic gait, lower limb hypertonia, nystagmus	mild abnormalities of RBCt, MCV, MCH
3/M	c.1442C>A (p.Thr481Asn)	15 years	2 months/ focal motor with asymmetric posturing	focal with impaired awareness and asymmetric posturing, focal to bilateral tonic-clonic/weekly	CBZ, CLB, PB, PER, STP, VGB, VNS	15 years: slow background, focal epileptiform discharges	4 years: thin CC, posterior predominant multifocal WM abnormalities, dysmorphic asymmetric lateral ventricles, enlarged cortical sulci	global profound DD, spastic asymmetric quadriparesis, severe cortical visual impairment	none
4/M[b]	c.130G>A (p.Val44Met)	12 years/ deceased at 12.5 years (pneumonia)	4 months/ focal	focal with impaired awareness; 9 months on: spasms and focal to bilateral tonic-clonic/daily; single episode of SE (14 months)	CBZ, CLB, KD, LTG, LEV, PRED, RFM, VGB, VPA, VNS	8 months–10 years: slow background, bilateral independent or multifocal discharges; epileptic spasms recorded	5 months, 7 years: thin CC, multifocal WM abnormalities, dysmorphic enlarged lateral ventricles, mild cortical and cerebellar atrophy, progressive trabecular bone thickening	global profound DD, wheelchair bound, cortical visual impairment, by 10 years knee fixed flexion contractures, dysphagia (PEG 5 years)	severe macrocytic anemia transfusion dependent

(*Continued on next page*)

Table 1. ***Continued***

Individuals' ID/gender	TMEM63B variant[a] (cDNA and protein)	Age at last follow-up/ death	Age at seizure onset/type	Seizure types/ severity during follow-up	Treatment ever tried (+ efficacy, +/− transient efficacy, − worsening or not tolerated)	EEG	Brain magnetic resonance imaging	Clinical neurological phenotype	Hematological findings
5/M	c.130G>A (p.Val44Met)	8 years	day 2/apnoeic	4 months: epileptic spasms; 7 years: focal hyperkinetic motor with impaired awareness/sz-free	CBZ(+), CLB, LEV, PB(+), TPM(+)	7 years: slow background, bilateral independent or multifocal discharges; focal szs recorded	1 week, 7 months, 2 years: thin CC, abnormal myelination, dysmorphic asymmetric lateral ventricles, enlarged extracerebral spaces, progressive posteriorly predominant WM abnormality, and cerebellar atrophy	global profound DD, severe cortical visual impairment, nystagmus, spastic quadriparesis, dysphagia (PEG 2 years)	jaundice at birth
6/F[b]	c.130G>A (p.Val44Met)	15 months/ deceased at 23 months (pneumonia in progressive respiratory failure)	day 10/ apnoeic	focal onset with impaired awareness, focal to bilateral tonic-clonic, epileptic spasms/ daily	Alimemazine, CBZ, CLB, PB(+/−), paraldehyde, PRED, TPM, VGB, VPA, VNS(+), biotin, pyridoxine	2–23 months: slow background, multifocal or generalized discharges with burst suppression; focal szs recorded	2 months: thin CC, enlarged extracerebral spaces, diffusely abnormal myelination	global profound DD, quadriparesis with generalized hypotonia, cortical visual impairment, nystagmus, dysphagia (PEG 16 months)	macrocytic anemia, transfusion dependent
7/M[a]	c.130G>A (p.Val44Met)	20 months	birth/apnoeic	2 weeks: stiffening episodes; 9 months: epileptic spasms/ sz-free	LEV, steroids, VGB	birth–20 months: normal background, then hypsarrhythmia, slow background, focal discharges	1 week, 5 months, 11 months: thin CC, widespread WM abnormalities, enlarged dysmorphic lateral ventricles, mild progressive cerebellar atrophy	global profound DD, asymmetric quadriparesis, generalized hypotonia, cortical visual impairment, nystagmus, dysphagia (no P EG yet)	scleralicterus

(*Continued on next page*)

Table 1. ***Continued***

Individuals' ID/gender	TMEM63B variant[a] (cDNA and protein)	Age at last follow-up/ death	Age at seizure onset/type	Seizure types/ severity during follow-up	Treatment ever tried (+ efficacy, +/− transient efficacy, − worsening or not tolerated)	EEG	Brain magnetic resonance imaging	Clinical neurological phenotype	Hematological findings
8/F	c.130G>A (p.Val44Met)	17 years	4 months/ infantile spasms	1 year: generalized tonic, focal motor with impaired awareness/daily	ACTH, CBZ, CLB, CZP, ESM, GBP, ivIg, LCM, LEV, PB, PER, PIR, PLP, PRM, STP, TPM, VPA, ZNS	4 months–12 years: hypsarrhythmia, then slow background, multifocal epileptiform discharges	4 months, 2 years, 10 years: thin CC, abnormal myelination, dysmorphic asymmetric lateral ventricles, enlarged extracerebral spaces, progressive widespread WM abnormality, ventricular dilatation, cerebellar atrophy, and trabecular bone thickening	global profound DD, quadriparesis, dysphagia (PEG 12 years)	severe anemia requiring occasional transfusions
9/M	c.130G>A (p.Val44Met)	15 years	2 years 6 months/ febrile seizures	3 years: epileptic spasms in small clusters/weekly	CZP, VPA	slow background, no epileptiform discharges in 4 EEG recordings	4 months: thin CC with absent splenium and delayed myelination; 6 years 7 months: increased signal of WM in watershed areas, generalized decrease of white matter volume	global profound DD, wheelchair bound, quadriparesis, pseudobulbar signs, jerky involuntary movements, stereotypical movements and behavior, dysphagia (PEG 3 years), cortical visual impairment, nystagmus	mild anemia
10/F	c.1377C>G (p.Asp459Glu)	3 years	2 weeks/focal	bilateral independent focal, epileptic spasms/daily	CBD, KD, LEV, VGB, VNS, ZNS	2–9 months: slow background, hypsarrhythmia, multifocal discharges; focal szs and epileptic spasms recorded	2 months: thin CC, enlarged extracerebral spaces, abnormal myelination more pronounced posteriorly, Rathke cleft cyst	global profound DD, quadriparesis, generalized hypotonia, cortical blindness with roving eye movements, dysphagia	mild macrocytic anemia

(*Continued on next page*)

Table 1. *Continued*

Individuals' ID/gender	TMEM63B variant[a] (cDNA and protein)	Age at last follow-up/ death	Age at seizure onset/type	Seizure types/ severity during follow-up	Treatment ever tried (+ efficacy, +/− transient efficacy, − worsening or not tolerated)	EEG	Brain magnetic resonance imaging	Clinical neurological phenotype	Hematological findings
11/M	c.1387G>A (p.Val463Ile)	7 years	2 years/focal	occasional focal with impaired awareness/during fever	VPA	4–6 years: normal background, bilateral independent discharges	6 years: multifocal, posteriorly predominant WM abnormality	global severe DD, motor impairment, generalized hypotonia	none
12/M	c.1387G>A (p.Val463Ile)	23 months	first few weeks/ myoclonic jerks	14 months; intractable focal seizures	LEV, CLB, ESM, CLZ, TPM(+/−), VPA(−)	14 months: normal background, generalized and focal discharges	14 months: mild prominence of ventricular system and extra-axial CSF spaces	global DD, dysphagia	none
13/F	c.1424_1426del (p.Ile475del)	16 years	6 months/ infantile spasms	tonic/daily; GTCs/ monthly	ACTH, CBD, CLB, CZP, LEV, LTG, OXC, TPM(−), VGB(−), VPA	4 months–16 years: hypsarrhythmia, then slow background, bilateral independent or multifocal discharges; epileptic spasms and tonic szs recorded	7 months, 2 years, 4 years, 8 years: thin CC, multifocal WM abnormalities, asymmetric dysmorphic lateral ventricles, progressive trabecular bone thickening	global profound DD, generalized hypotonia, microcephaly, visual impairment, nystagmus, squint, spastic quadriparesis, dysphagia (PEG 12 years)	severe hemolytic anemia, transfusion dependent
14/M	c.1738G>A (p.Gly580Ser)	5 years	10 months/ focal	GTCs/occasional during fever	VPA	2 years: slow background, focal discharges	1 year 7 months: thin CC, widespread WM abnormality, especially periventricular, asymmetric dysmorphic lateral ventricles, mild cerebellar atrophy	global profound DD, spastic quadriparesis, axial hypotonia, upper limb dystonia, visual impairment, dysphagia (PEG 3 years)	none
15/F	c.1738G>T (p.Gly580Cys)	30 years	3 years/focal	focal with impaired awareness, GTCs/ yearly	CBZ, CZP, PHT(+), VPA, ZNS	15 years: slow background, focal discharges; focal szs recorded	15 years, 21 years, 24 years, 27 years, 28 years: thin CC, widespread WM abnormality, especially periventricular/ posterior, progressive cerebellar atrophy, and trabecular bone thickening	global moderate DD, cerebellar ataxia, tremor, dysarthria, limited mobility, bipolar disorder	mild hyperbilirubinemia

(*Continued on next page*)

Table 1. ***Continued***

Individuals' ID/gender	TMEM63B variant[a] (cDNA and protein)	Age at last follow-up/ death	Age at seizure onset/type	Seizure types/ severity during follow-up	Treatment ever tried (+ efficacy, +/− transient efficacy, − worsening or not tolerated)	EEG	Brain magnetic resonance imaging	Clinical neurological phenotype	Hematological findings
16/F	c.1979G>C (p.Arg660Thr)	25 years	11 months/ focal	focal with posturing and impaired awareness, recurrent SE/yearly	CBZ(−), LMT(−), OXC, PB(−), TPM, VNS(+)	17 months–22 years: background mildly abnormal, diffuse beta activity, multifocal discharges; focal szs recorded	1 year, 2 years, 10 years: thin CC, multifocal WM abnormality	global moderate DD, spastic quadriparesis, ASD	macrocytic anemia
17/M	c.2089T>C (p.Phe697Leu)	15 years	11 months/ focal	focal with eye deviation; jerking, GTCs, recurrent SE/sz-free at last FU	CLB, LTG(−), LEV(−), OXC, PHT, VPA	5–17 months: normal background; focal discharges	1 year, 12 years: thin CC, abnormal myelination, colpocephaly, dysmorphic lateral ventricles, increased WM signal with posterior/ periventricular predominance	global, severe DD, toe walking, ASD	none

Abbreviations and symbols: ASD, autism spectrum disorder; CBD, cannabidiol; CBZ, carbamazepine; CC, corpus callosum; CLB, clobazam; CZP, clonazepam; DD, developmental delay; ESM, ethosuximide; F, female; GBP, gabapentin; GTCS, generalized tonic-clonic seizures; ivIg, intravenous immunoglobulin; KD, ketogenic diet; LCM, lacosamide; LEV, levetiracetam; LTG, lamotrigine; M, male; MCH, mean corpuscular hemoglobin; MCV, mean corpuscular volume; MDZ, midazolam; NA, not available; OXC, oxcapazepine; PB, phenobarbital; PEG, percutaneous endoscopic gastrostomy; PER, perampanel; PHT, phenytoin; PIR, piracetam; PLP, pyridoxal 5′-phosphate; PRED, prednisolone; PRM, primidone; RBCs, red blood cells; RFM, rufinamide; SE, status epilepticus; STP, stiripentol; sz, seizure; TGP, targeted gene panel; TPM, topiramate; VGB, vigabatrin; VNS, vagus nerve stimulation; VPA, valproic acid; WM, white matter; ZNS, zonisamide.

[a]Variants' nomenclature is based on the GenBank: NM_018426.3 reference sequence.

[b]IDs 4, 6, and 7 are mentioned in Cacheiro et al.[14] (Table S8: DDD subject 1, 100KGP subject 2, and[100KGP] subject 1); treatment ever tried: +, efficacy; +/−, transient efficacy; −, worsening or not tolerated.

All individuals (17/17, 100%) had global developmental delay, with moderate-to-profound intellectual disability and severe motor impairment; only two had developed communicative language skills (2/17, 12%). Severe dysphagia was present in 11 individuals (11/17, 65%), requiring a percutaneous endoscopic gastrostomy (PEG) insertion in eight (8/17, 47%). In 12 individuals (12/17, 71%), clinical history revealed hematological abnormalities resulting in abnormal hemoglobin levels, often with macrocytosis and signs of hemolysis (hyperbilirubinemia, jaundice, hepatosplenomegaly) with a fluctuating course. In four of the 12 individuals (4/12, 33%) with hematological abnormalities, three of whom were carrying the recurrent c.130G>A (p.Val44Met) variant, anemia was severe and required blood transfusions (IDs 4, 6, 8, and 13). In ID 4, peripheral blood film showed abnormally shaped red blood cells (RBCs) with elliptocytes and increased stomatocytes. Bone-marrow biopsy was performed in two individuals (IDs 4 and 8) with signs of hemolysis in both and evidence for hematopoiesis and myelodysplastic syndrome with aplastic anemia in one (ID 8, Figure S1). Auxological parameters at birth were normal in most individuals (Table S2). Three individuals (3/17, 18%) had died prematurely due to pneumonia (IDs 1, 4, and 6; Table 1).

Prompted by the evidence for progressive hearing loss in *Tmem63b*-deleted mice,[4] we investigated whether any signs of hearing impairment were present in our cohort. Eleven out of 17 (65%) individuals received formal hearing tests (Table S2) with abnormal results in two (IDs 15 and 16; 2/11, 18%). In a further individual (ID 10), hearing impairment was suspected on clinical ground but not formally tested.

MRI findings

All individuals had at least one brain MRI scan at 1.5 or 3T between ages 1 week and 28 years, and 11 individuals were studied with two or more scans taken 6 months to 13 years apart (Table 1 and Figure 1). MRI revealed an association of multiregional or widespread white matter signal abnormalities, dysmorphic lateral ventricles, thinning of corpus callosum (17/17, 100%), cerebellar atrophy (8/17, 47%), and atrophy of the cerebral cortex (8/17, 47%).

All the 11 individuals for whom repeated MRIs were available for comparison (IDs 1, 2, 4, 5, 7–9, 13, and 15–17) exhibited clear morphological or signal signs resulting from the combination of maturational and disease-related progressive changes. For example, when cerebellar atrophy was present, there had always been evidence of atrophy progression from initial to follow-up imaging (IDs 1, 2, 4, 5, 7, 8, and 15). White matter signal abnormalities (always present) appeared in early scans as severely delayed myelination that was better appreciated with T2-weighted imaging and later evident as diffuse or more circumscribed areas of high-signal intensity changes in fluid attenuated inversion recovery (FLAIR) (see IDs 1, 5, 7, and 8 in Figure 1). In the only individual who had received control MRI scans at different adult ages (ID 15), cerebellar and white matter changes continued to worsen between age 21 and 28. Overall, white matter abnormalities, ventricular shape, and thinning of the corpus callosum exhibited similar longitudinal changes. Signs of progression of cortical atrophy were minor, if any, and proportional to overall volume shrinking. MRI also showed progressive thickening of the trabecular (spongy) bone of the skull in five individuals (5/17, 29%; IDs 4, 8, 13, and 15 in Figure 1; ID 9, not shown), four of whom had anemia (IDs 4, 8, 9, and 13), with a myelodysplastic disorder in three (IDs 4, 8, and 13), while one had experienced episodes of hyperbilirubinemia (ID 15).

Genetic findings

In these 17 individuals, we identified ten distinct *TMEM63B* variants (Table 1 and Figure 2) including nine missense substitutions and one in-frame deletion. None of them were present in publicly available allele frequency databases, such as gnomAD and TOPMed, or in our internal dataset, and all were predicted to be damaging by multiple prediction tools (Table S3). Available gene constraint scores from gnomAD indicate that *TMEM63B* is globally highly intolerant to both loss-of-function (LoF; pLI score = 1.00; observed/expected [o/e] LoF = 0.07) and missense (Z score = 4.22; o/e missense = 0.475) variants. In addition, all variants were in regions of the protein predicted to be intolerant to missense variations according to region-level metrics (Figures 2B and S2) and involved amino acids highly conserved among the vertebrate orthologs of the protein (Figure 2C, Table S3), as well as the paralogs *TMEM63A* and *TMEM63C* (Figure S3).

We noticed a complementary linear distribution on the protein sequence of the *TMEM63B* variants in our cohort versus the gene variants in the reference population from gnomAD. The latter were enriched in exons 3–14 and 22–24 and substantially depleted in exons 15–21, where our variants clustered (Figures 2B and S2). This observation, supported by the local constraint metrics provided by multiple tools, suggests an increased selective pressure in the region of the gene corresponding to the seventh transmembrane (TM) domain region RSN1_7TM (PF02714). This domain is conserved among osmosensitive calcium-permeable cation channels.[16]

The p.Val44Met variant was recurrent in seven unrelated individuals (IDs 1, 4–9), the c.1387G>A (p.Val463Ile) in two (IDs 11 and 12), and two different changes affected the same residues in two individuals (c.1738G>A [p.Gly580Ser] in ID 14 and c.1738G>T [p.Gly580Cys] in ID 15). Eight of the affected residues are fully conserved from human to zebrafish (Val44, Arg433, Asp459, Val463, Thr481, Gly580, Arg660, and Phe697), and one is fully conserved up to chicken (Ile475). In addition, six out of nine affected residues are fully conserved among all the three paralogs' sequences (Val44, Asp459, Val463, Gly580, Arg660, and Phe697), and three (Arg433, Thr481, and Ile475) are fully conserved in two among three paralogs and they maintain similar properties in the third paralog (Figure S3).

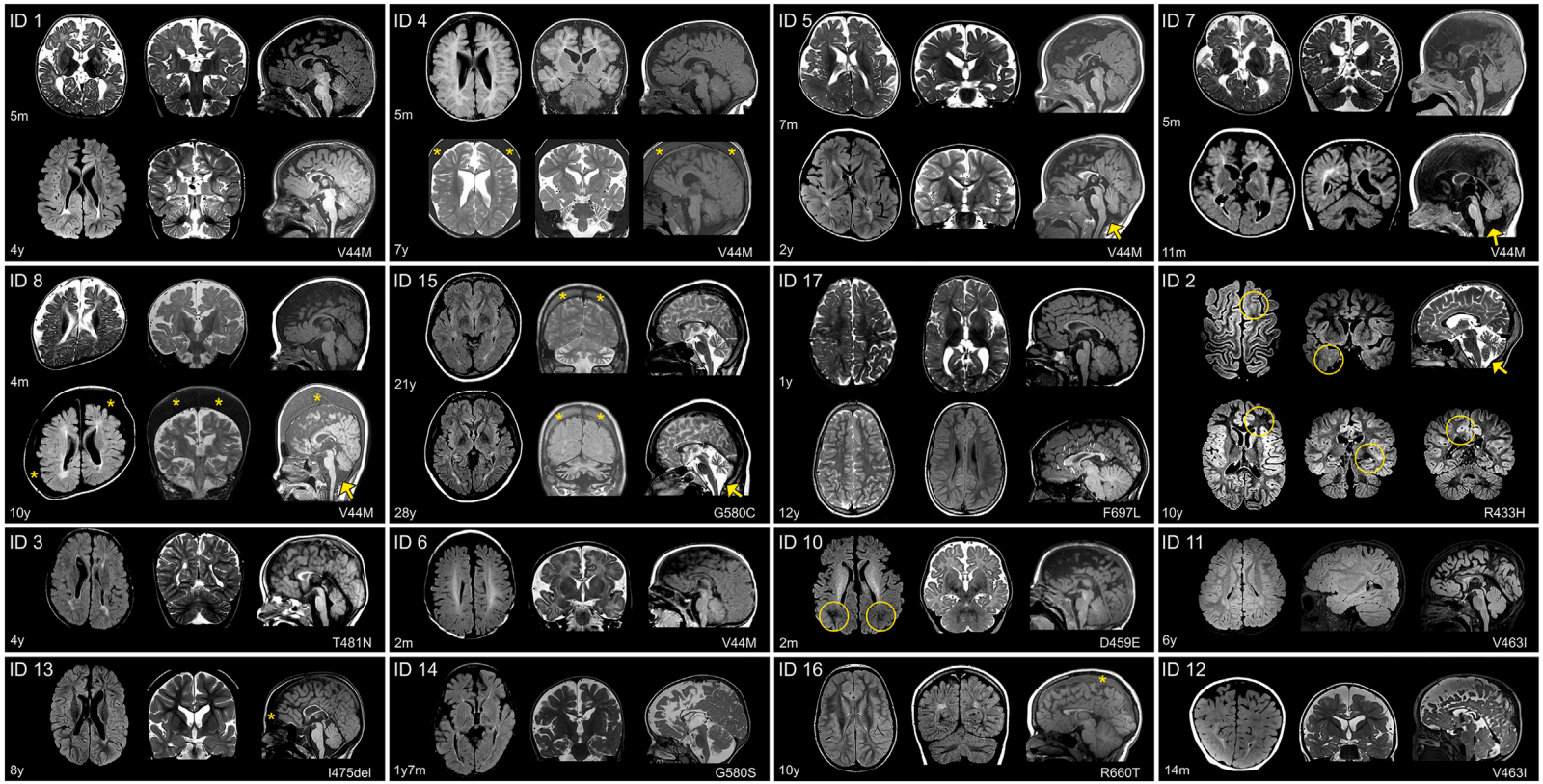

Figure 1. Brain MRI in 16 individuals with *TMEM63B* pathogenic variants

Individuals' ID is shown in the upper left corner. For each individual, the corresponding *TMEM63B* variant is reported in the lower right corner. For IDs 1, 4, 5, 7, 8, 15, and 17, two sets of comparative images are presented, taken respectively from the initial and follow-up investigation. For IDs 2, 3, 6, 10, 11–14, and 16, only one set of images is presented. For ID 2 we included additional images, illustrating suspected areas of focal cortical dysplasia (circles). Structural abnormalities include a combination of white matter (WM) abnormalities, dysmorphic lateral ventricles, thinning of corpus callosum (CC), and cortical and cerebellar atrophy that are variably distributed. In ID 1, MRI at age 5 months shows increased extracerebral spaces with enlarged cortical sulci, thin CC with colpocephaly, and high signal intensity of the hemispheric WM, consistent with abnormal myelination. At age 4, enlarged extracerebral spaces and thinning of the CC are less prominent but there is a definite high signal abnormality of the WM, with dysmorphic lateral ventricles, and mild atrophy of the cerebellar cortex. In ID 4, after a first MRI at age 5 months only showing reduced volume of the frontal lobes, a follow-up scan at 7 years revealed a progressive change in shape of the lateral ventricles and CC, revealing WM suffering with mild atrophy of the cerebellar cortex. In IDs 5 and 8, changes that occurred from age 7 months to age 2 years (ID 5) and from age 4 months to 10 years (ID 8) are comparable with those observed in ID 1. The abnormal ventricular shape causes ventricular asymmetry in these individuals. Cerebellar atrophy is indicated by arrows. In ID 7, a second MRI at age 11 months confirms the severe WM abnormality with dilated ventricles and thin CC and reveals mild progressive cerebellar atrophy (arrow). In ID 15, imaged twice 7 years apart, MRI shows as WM changes and cerebellar atrophy continued to progress after age 21 (arrow). In ID 17, only minor changes occurred between age 1 year and 12 years. At 1 year, there were areas of abnormal myelination, especially on the right hemisphere, with thin CC and colpocephaly. At age 12, the CC remained thin but because of maturation processes was thicker than before and ventricular dilatation less prominent, with mild peritrigonal high signal intensity. In ID 2, brain MRI taken at 10 years shows bilateral patchy WM abnormalities highlighted by a circle in the left frontal and right temporal regions. This finding, in association with focal seizures, had raised the suspicion of areas of focal cortical dysplasia. Additional findings include ventricular asymmetry, thin CC, and progressive cerebellar atrophy. In ID 3, imaged at 4 years, there are multifocal high signal WM changes with dysmorphic and asymmetric lateral ventricles, thin CC, and enlarged cortical sulci. IDs 6 and 10, both imaged at age 2 months, exhibited increased extracerebral spaces with enlarged sulci, thin CC, and reduced signal intensity of the WM, consistent with abnormal myelination (ID 10, circles). In ID 11, at age 6 years, there were multifocal areas of WM abnormalities without atrophic changes. In ID 12, at age 14 months, there is already an obvious combination of dilated extracerebral spaces and ventricles with thin CC and high signal abnormality in the posterior WM. IDs 13, 14, and 16 imaged between 1 year 7 months and 10 years show similar findings, slightly varying in severity and including a thin CC, areas of abnormal signal intensity of the WM with posterior predominance in all, dilated asymmetric ventricles (IDs 13 and 14), and mild cerebellar atrophy (ID 14). In IDs 4, 8, 13, 15, and 16, thickening of the trabecular (spongy) bone of the skull (indicated by the asterisks) is suggestive of a blood disorder.

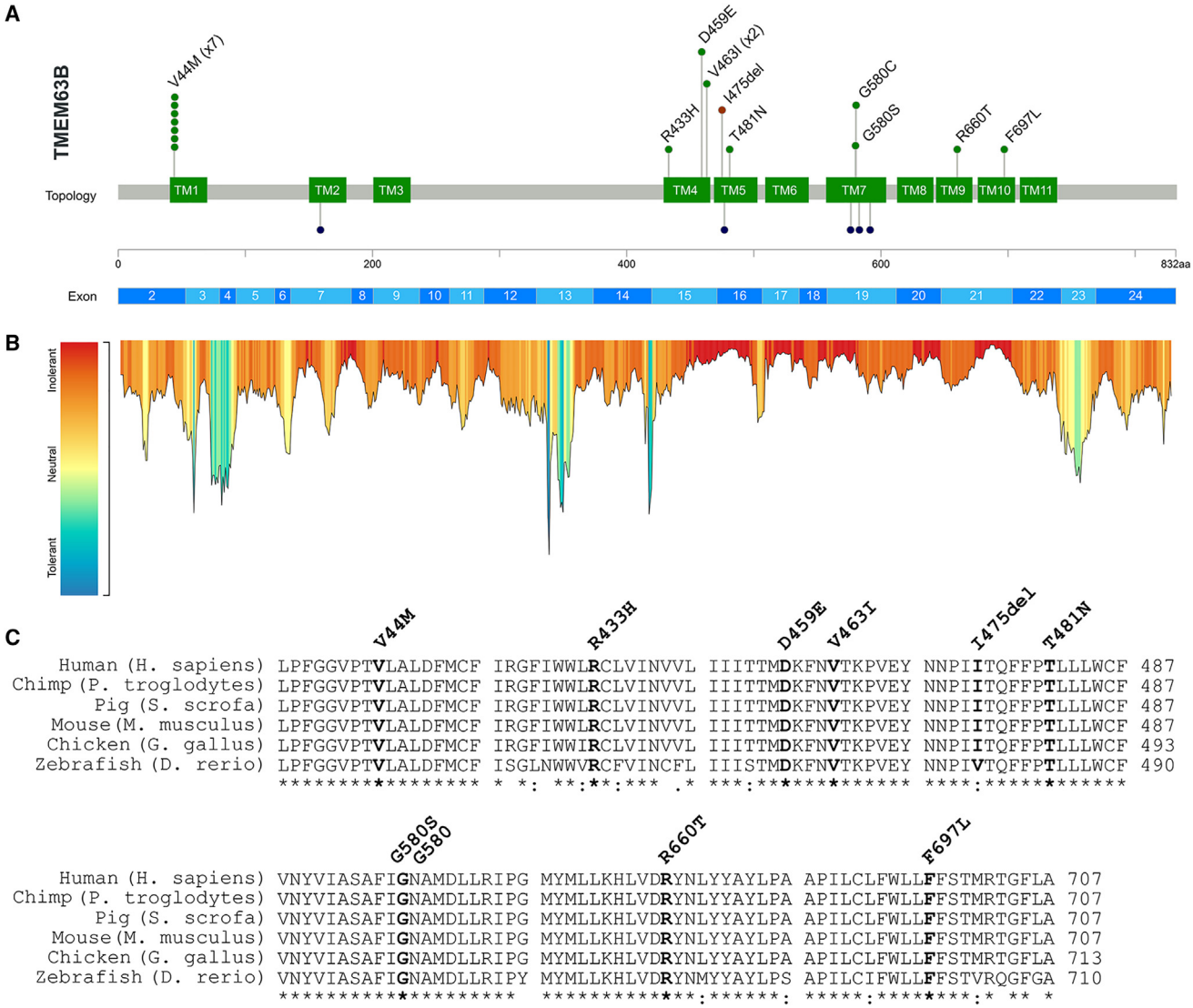

Figure 2. Genetic results

(A) The lollipop diagram shows the distribution of the TMEM63B variants observed in our cohort on the linear protein map and relative to the *TMEM63B* exons (top, based on NM_018426.3 reference sequence). The variants are represented as green (missense substitutions) or brown (in-frame deletion) dots and all map in the transmembrane helices TM1, TM4–7, and TM9–10 (green boxes). The p.Val44Met (V44M) and the p.Val463I (V463I) are recurrent in seven and two individuals, respectively, as illustrated by the number of green dots. At the bottom of the diagram, the dark blue dots represent the residues affected by missense variants in *TMEM63A* (five variants in six unrelated individuals: p.Gly168Glu [G168E], p.Ile462Asn [I462N], p.Gly553Val [G553V], p.Tyr559His [Y559H], p.Gly567Ser [G567S]).[6–8]
(B) Tolerance landscape plot of the TMEM63B protein provided by the MetaDome web server (https://stuart.radboudumc.nl/metadome/). The tool identifies regions of low tolerance to missense variations based on the local non-synonymous over synonymous variants ratio from gnomAD.[15] All variants in our cohort are contained in intolerant/highly intolerant regions (in red) of the landscape.
(C) Multiple sequence alignment shows the protein sequence of the human TMEM63B protein (NP_060896.1) and of its orthologs in five different vertebrate species (*Pan troglodytes*, *Sus scrofa*, *Mus musculus*, *Gallus gallus*, *Danio rerio*) with the mutated residues in bold. The details of the TMEM63B variants in the cohort are displayed above the alignments. The asterisk below the sequence indicates positions that have a single, fully conserved residue between all the input sequences, the colon indicates conservation between groups of strongly similar properties, and the period indicates conservation between groups of weakly similar properties.

The *TMEM63B* variant occurred *de novo* in the 16 individuals for whom parental DNA was tested. Individual 10 was born through egg donation; therefore, maternal DNA was not available for analysis. The variant was absent from the DNA of the father and of the healthy dizygotic twin.

Based on both *in silico* analyses using sequence data and the functional studies described below, we interpreted all variants as detrimental for the function of the protein.

In 13/17 (77%) individuals, we did not identify additional clinically relevant variants (Table S2). In ID 12, a *de novo TSC1* variant was associated with macrocephaly with no other signs of tuberous sclerosis complex (TSC1 [MIM: 191100]). In three more individuals (IDs 9, 16, and 17), additional variants were identified, which were

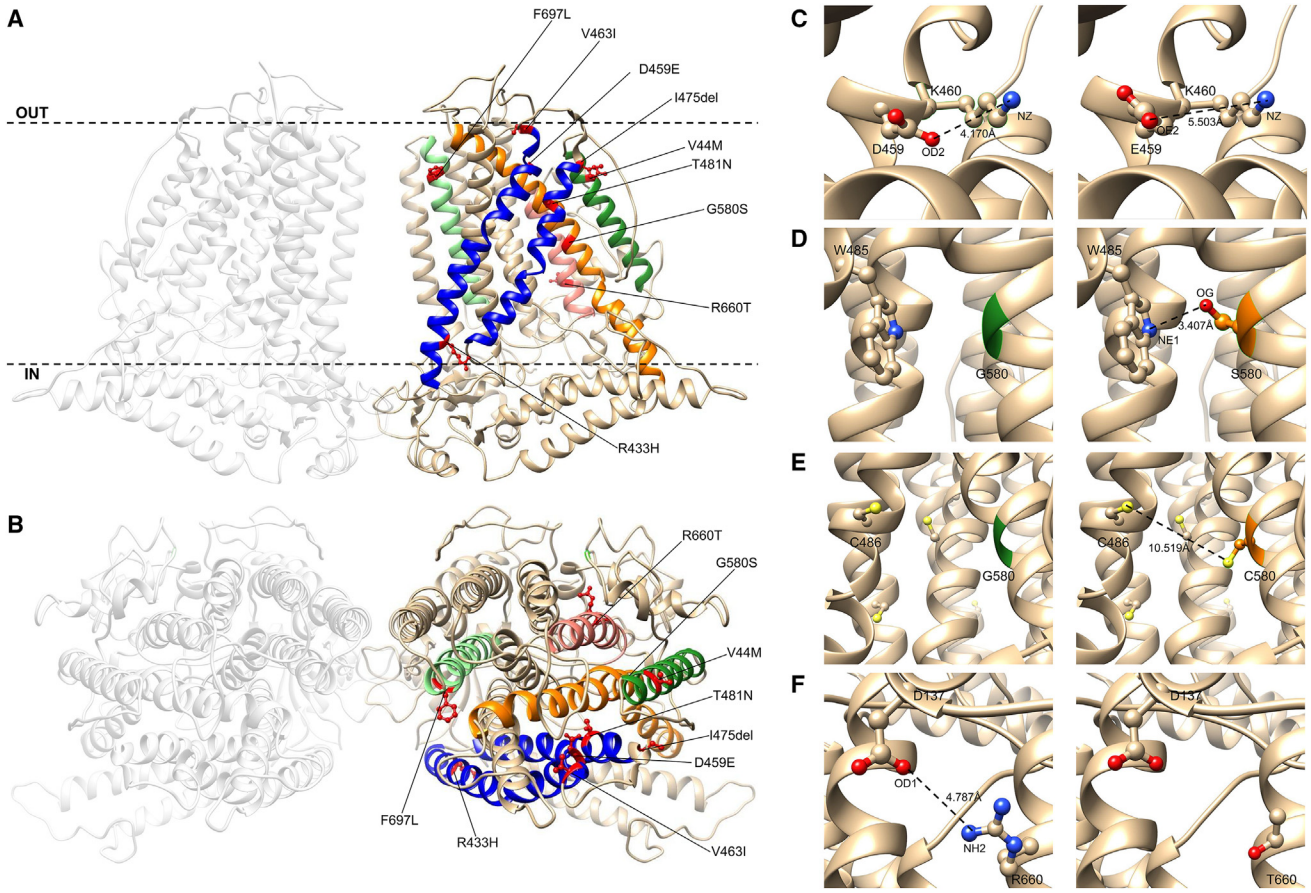

Figure 3. Structural consideration of TMEM63B pathogenic variants

(A and B) View of the predicted tridimensional protein structure of TMEM63B from the membrane plane (A) and the extracellular side (B). All the variants in our cohort map into a transmembrane (TM) helix: p.Val44Met (V44M) in TM1 (dark green helix), p.Arg433His (R433H), p.Asp459Glu (D459E), p.Val463Ile (V463I), p.Ile475del (I475del), and p.Thr481Asn (T481N) in TM4 and TM5 (blue helices), p.Gly580Ser (G580S) in TM7 (orange helix), p.Arg660Thr (R660T) in TM8 (pink helix), and p.Phe697Leu (F697L) in TM9 (light green helix). Dotted line in (A) indicates the plasma membrane, OUT the extracellular side and IN the intracellular (cytoplasmic) side. Details of selected variants are provided in the inlets.

(C) Predicted structural change induced by the D459E substitution. The OD2 atom of Asp459 is predicted to form a buried salt bridge with NZ atom of Lys460 (K460). The substitution of an aspartic acid with a glutamic acid at position 459 increases the distance between the NZ atom of Lys460 and the closer oxygen atom (OE2) available to make a salt bridge, breaking this bond.

(D) Predicted structural change induced by the G580S substitution. The substitution of a glycine (green) with a bulkier amino acid (serine, orange) changes the RSA of the amino acid at position 580 (5.9%–3.8%). In addition, OG atom of Ser580 might form a salt bridge with NE1 atom of Trp485 (W485) and help in stabilizing the structure of the pore.

(E) Predicted structural change induced by the G580C substitution. The substitution of a glycine (green) with a bulkier amino acid (cysteine, orange) changes the RSA of the amino acid at position 580 (5.9%–3.7%). Although the substitution introduces an amino acid with a free SH group that can make disulphide bonds with other amino acids with free SH groups (depicted as yellow spheres), the distance between C580 and the closer amino acid with a free SH group (C486, 10.519 Å) is too big to allow the making of such type of bond.

(F) Predicted structural change induced by the R660T substitution. The substitution of a buried charged residue (arginine) with an uncharged residue (threonine) at position 660 disrupts a salt bridge formed by NH2 atom of Arg660 and Asp137 (D137).

either classified as variants of uncertain significance (VOUSs) or reported as unsolicited findings not related to the phenotypic spectrum presented here (Table S2).

Structural considerations

Because crystallographic data are not yet available for TMEM63B, we can only access information about the protein topology based on its partial homology with the plants' OSCAs for a subset of whom crystallographic data are available.[2,17,18] As the percentage of identity in protein sequence between mammals TMEM63A–C proteins and OSCAs is around 20%,[1] mapping our variants on these structures would be inaccurate. Aware of the limitations of prediction tools in regions of low homology, we mapped our variants on the structure exhibiting more homogeneous resolution across the protein, including both the TM helices and the intracellular domains (Figures 3 and S4). In our model, 81% of residues had >90% confidence, including all those affected by variants in our cohort, all affecting a predicted TM helix (Figures 2A, 3A, and 3B).

Five variants fell in TM4 (c.1298G>A [p.Arg433His], c.1377C>G [p.Asp459Glu], and c.1387G>A [p.Val463Ile]) or TM5 (c.1424_1426del [p.Ile475del] and c.1442C>A [p.The481Asn]) (Figures 3A and 3B, blue helices), whose tilting and rearrangement upon osmotic stimulus plays a role in channel opening in *Oryza sativa* OSCA1.2 protein.[18] The remaining variants mapped in TM1 (p.Val44Met), TM7 (p.Gly580Ser and p.Gly580Cys), TM8 (c.1979G>C [p.Arg660Thr]), and TM9 (c.2089T>C [p.Phe697Leu]). All but the recurrent p.Val44Met variant are in the Pfam-classified domain RSN1_7TM,[16] and six of them affect the predicted pore-forming TM4–TM8 helices.[2]

The p.Val44Met (IDs 1 and 4–9) lies in a region with limited sequence homology between OSCAs and TMEM63A–C and for which available OSCA structures have low resolution.[2,17] The valine to methionine substitution involves two amino acids with similar properties (Grantham distance 21; scale 0–215) and mass. The TM1 helix is located on the external surface of the channel and is not directly involved in the predicted pore, but it seems to be rather involved, together with TM7, in the sensitivity to membrane stretching (Figure 2).[2,17]

In a FoldX-based model, Met44 is predicted to make van der Waals contacts with Gln477, Phe478, and Thr481, all mapping on the TM4 helix (Figure S5). Because the free energy change associated with p.Val44Met is negative (−1.46, calculated by FoldX), we hypothesize that this substitution may stabilize the protein structure.

We estimated evolutionary conservation and role of the mutated residues by ConSurf, which confirmed that all changes affected highly conserved residues with predicted functional and/or structural role (Figure S6; Table S4).

We also evaluated the structural impact of the nine distinct missense variants in our cohort by using the Missense3D tool[19] and found that eight of nine may affect the protein structure, although limitedly, via changes in cavities volume (7/8), residues accessibility (3/8), and breakage of non-covalent bonds (2/8) (Table S4). The p.Asp459Glu substitution (ID 10) disrupts a salt bridge formed between OD2 atom of Asp459 and NZ atom of Lys460 (distances: 4.168 Å between OD2 atom of Asp450 and NZ atom of Lys460, 5.503 Å between OE2 atom of Glu450 and NZ atom of Lys460) (Figure 3C). The p.Gly580Ser substitution (ID 14) replaces a buried glycine, with a residue solvent accessibility (RSA) of 5.9%, with a buried serine with an RSA of 3.8%. In addition, OG atom of Ser580 might form a salt bridge with NE1 atom of Trp485 (W485), possibly stabilizing the structure of the pore (Figure 3D). Substitution of the Gly580 amino acid with a cysteine (p.Gly580Cys, ID 15) introduces a bulkier residue at position 580 and changes its RSA from 5.9% to 3.7%. Although the free thiol (SH) residue of Cys580 can make disulphide bonds with other amino acids with free SH residues, the distance between Cys580 and Cys486, which is the closer amino acid with a free SH residue (10.519 Å; Figure 3E), does not allow the making of disulphide bonds. The p.Arg660Thr variant (ID 16) replaces a buried charged arginine (RSA 5.6%) with an uncharged threonine. This substitution also disrupts a salt bridge between NH_2 group of Arg660 and OD1 atom of Asp137 (distance: 4.787 Å) (Figure 3F). For p.Val44Met, p.Arg433His (ID 2), p.Val463Ile (IDs 11 and 12), and p.Phe697Leu (ID 17), Missense3D suggests only mild alterations of the cavity volume (<70 $Å^3$) without significant structural changes, which might still influence the overall stability of the protein (Table S4). It has indeed been demonstrated that cavities in membrane proteins play a pivotal role in balancing stability and flexibility, impacting protein function.[20] For the p.The481Asn (ID 3), which according to ConSurf affects a predicted structural residue, Missense3D did not indicate clear structural damage but could calculate cavity volume in the mutant structure. As for the in-frame deletion variant p.Ile475del (ID 13), Phyre2 modeling did not predict gross alterations of the secondary structure.

Post-transcriptional editing in *TMEM63B* mRNA from human cerebral cortex and selection of variants for *in vitro* functional studies

In the mouse brain, the *Tmem63b* isoform lacking exon 4 is the most expressed during all developmental stages, and the Q/R editing at exon 20 is absent in the early brain but increases with age, reaching ∼80% in *Tmem63b* mRNA in the adult cortex.[10]

To characterize TMEM63B expression profile in humans, we reverse-transcribed RNA from an adult human cerebral cortex sample into cDNA and amplified by PCR the region around exon 4 (Figure S7A). We found that exon 4 was missing in 80% of *TMEM63B* mRNA (Figures S7B and S7C). We further characterized the Q/R editing at exon 20 in long and short *TMEM63B* isoforms by PCR and Sanger sequencing and found that the editing occurred only in the short isoform (Figures S7D and S7E). Both the exon 4 splicing and Q/R editing findings are in line with previous observations in mice,[10] except for lower Q/R editing occurrence in the adult human cortex (∼40%) (Figure S7E).

Collectively, these data prompted us to study the effects of selected *TMEM63B* variants *in vitro* by modeling them in the short non-edited isoform, which is likely the most abundant in the developing cortex.

For functional studies in Neuro2A cells, we selected six missense variants (p.Val44Met, p.Arg433His, c.1442C>A [p.Thr481Asn], p.Gly580Ser, c.1979G>C [p.Arg660Thr], and c.2089T>C [p.Phe697Leu]), each affecting a distinct TM domain of the channel (Figure 2A). We also included in the experiments the truncating variant c.973C>T (p.Arg325*) as a negative control. We became aware of such variant through our matchmaking initiative, as it was found at the homozygous state in an individual with an unrelated phenotype and was heterozygous in both parents who were healthy (unpublished data). The p.Arg325* is located in exon 12 of 24 and predicted to result in nonsense-mediated decay (NMD) of the aberrant mRNA.

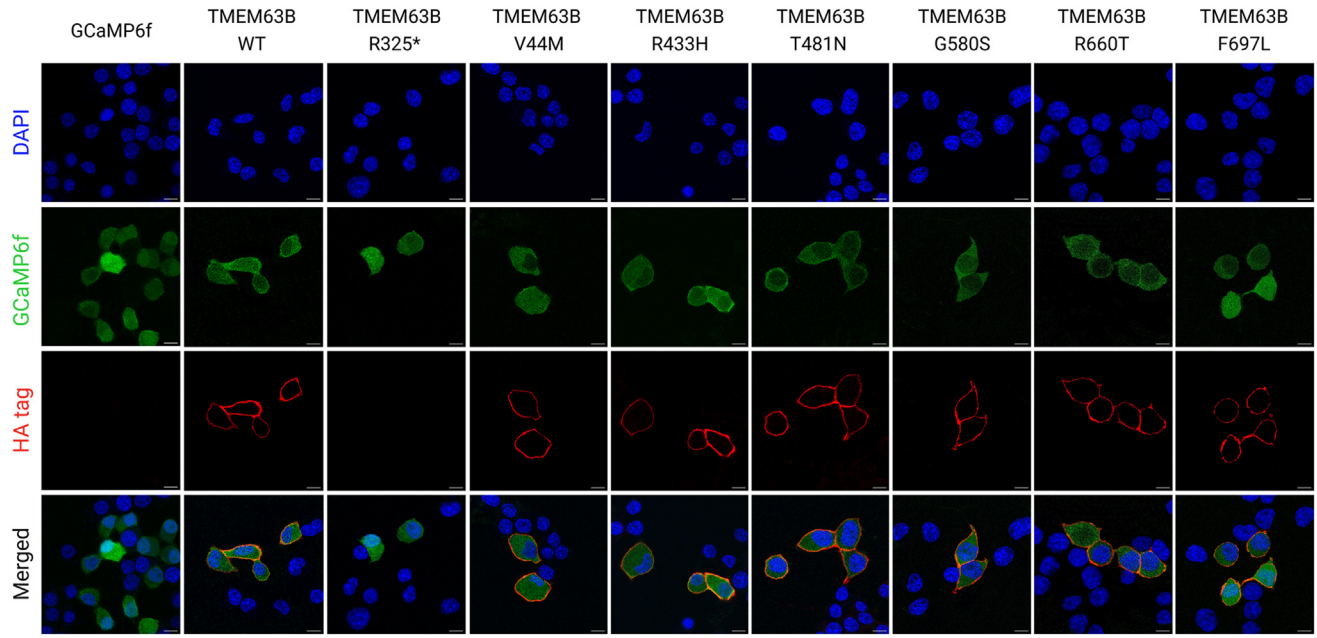

Figure 4. Immunocytochemistry to assess TMEM63B localization at the plasma membrane
Confocal microscopy photographs of Neuro2A cells transfected with GCaMP6f empty vector, TMEM63B WT, or mutant plasmids and analyzed 48 h post-transfection. Transfected cells express the GCaMP6f protein, which fluoresces in the green channel. Cells were stained with primary anti-HA tag antibody, secondary Alexa Fluor 555 antibody, and DAPI. Scale bar = 10 μm.

p.Val44Met, p.Arg433His, p.Thr481Asn, p.Gly580Ser, p.Arg660Thr, and p.Phe697Leu do not affect TMEM63B localization at the plasma membrane

The TMEM63B channel normally localizes at the plasma membrane level.[21,22] To address the impact of p.Val44Met, p.Arg433His, p.Thr481Asn, p.Gly580Ser, p.Arg660Thr, and p.Phe697Leu on TMEM63B localization, we performed immunocytochemistry in Neuro2A cells transfected with GCaMP6f plasmids overexpressing either wild-type (WT) or mutant hemagglutinin (HA)-tagged TMEM63B and GCaMP6f empty vector as control.

In WT- and mutant-expressing Neuro2A cells, TMEM63B was correctly localized at the membrane level (Figure 4). As expected, we did not observe TMEM63B expression in control GCAMP6f and in p.Arg325*-expressing cells. These findings suggest that the six missense variants we studied exert their effect by altering the channel function without impacting localization on the plasma membrane.

p.Val44Met, p.Arg433His, p.Thr481Asn, p.Gly580Ser, p.Arg660Thr, and p.Phe697Leu affect TMEM63B conductance

In physiological conditions, TMEM63B operates as a non-selective cationic channel activated by mechanical and osmotic stimuli.[1,4] To address the impact of the selected p.Val44Met, p.Arg433His, p.Thr481Asn, p.Gly580Ser, p.Arg 660Thr, and p.Phe697Leu variants on channel properties, we applied a set of electrophysiological protocols previously implemented to characterize WT TMEM63B *in vitro*.[4] In transfected Neuro2A cells, we initially recorded whole-cell currents elicited by a −80 to +80 mV voltage ramp protocol in isotonic conditions (300 mOsm/L extracellular solution) and then imposed a hypo-osmotic stimulus by switching to a 170 mOsm/L solution.

In cells expressing each of the selected *TMEM63B* variants, a −80 mV step imposed under isotonic conditions elicited a stable inward current that was absent in TMEM63B WT, control GCAMP6f, and p.Arg325*-expressing cells (Figures 5A and 5B). Outward currents elicited at +80 mV were also enhanced in cells expressing p.Val44Met, p.Arg433His, p.Thr481Asn, p.Gly580Ser, p.Arg660Thr, and p.Phe697Leu compared with controls (Figure 5C). These six variants also caused a significant depolarization of the reversal potential, as shown by the current-voltage (I/V) relationship (Figures 5A and 5D).

Under hypo-osmotic conditions, a −80 mV step elicited an inward current in cells expressing either the WT or mutant TMEM63B, while no current was generated in control cells (Figure S8). In most cases, cells underwent massive swelling and eventually burst, as previously reported.[4] WT- and mutant-expressing cells that sustained the hypo-osmotic shock and reached the plateau currents exhibited similar current amplitudes (Figures S8A and S8B). The overall increase in currents observed at −80 mV, expressed as the delta (Δ) between currents measured under hypo-osmotic and isotonic conditions, was larger in WT- than in mutant TMEM63B-expressing cells (Figure S8C), as might be expected by an inward leak current under isotonic conditions in the mutant.

Overall, these results show that p.Val44Met, p.Arg433His, p.Thr481Asn, p.Gly580Ser, p.Arg660Thr, and p.Phe697Leu alter channel conductance, resulting in partial channel

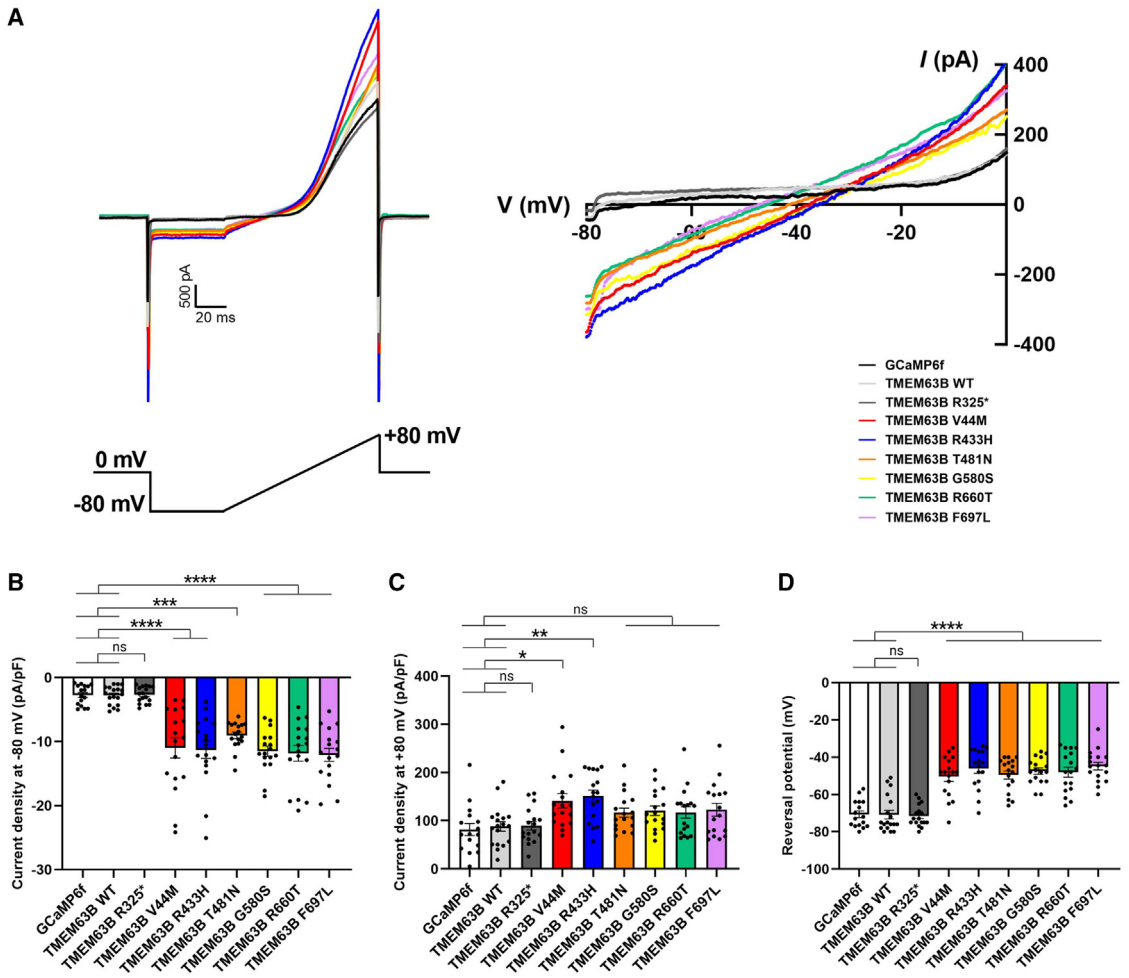

Figure 5. Electrophysiological recordings on transfected Neuro2A cells

(A) Left: representative raw traces of TMEM63B-mediated currents registered under isotonic condition in Neuro2A cells transfected with GCaMP6f, TMEM63B WT, or mutant plasmids. Cells were held at 0 mV and recorded with a ramp protocol from −80 mV to +80 mV, 100 ms duration, 0.1 Hz. Right: current-voltage (I/V) relationship showing variant-induced change in reversal potential.

(B and C) Quantification of whole-cell current density at −80mV (B) and +80mV (C) (GCaMP6f = 16 cells, TMEM63B WT = 18 cells, TMEM63B R325*, V44M, R433H, T481N, G580S, R660T, and F697L = 17 cells; ****$p < 0.0001$, ***$p < 0.001$, **$p < 0.01$, *$p < 0.05$, ns = not significant, Kruskal-Wallis and Dunn's multiple comparisons tests).

(D) Quantification of reversal potential (GCaMP6f = 16 cells, TMEM63B WT = 18 cells, TMEM63B R325*, V44M, R433H, T481N, G580S, R660T, and F697L = 17 cells; ****$p < 0.0001$, one-way ANOVA and Tukey's multiple comparison test). Data are expressed as mean ± SEM.

activation in physiological conditions, without altering the maximal channel conductance under hypo-osmotic stimulation.

p.Val44Met, p.Arg433His, and p.Thr481Asn affect calcium permeability

Previous experiments conducted in Neuro2A cells demonstrated that hypo-osmotic challenges trigger cationic currents across the TMEM63B channel with hyposmolarity-induced Ca^{2+} influx.[4] To determine whether the TMEM63B variants affect the hyposmolarity-induced Ca^{2+} response, we co-expressed in Neuro2A cells the Ca^{2+} sensor GCaMP6f and either WT TMEM63B or one of the three mutants p.Val44Met, p.Arg433His, and p.Thr481Asn. We selected these variants based on their recurrence in multiple individuals with overlapping clinical features (p.Val44Met) and location in critical TM helices TM4 (p.Arg433His) and TM5 (p.Thr481Asn), whose rearrangement is implicated in channel opening.[18]

We performed calcium imaging under a confocal microscope in a recording chamber equipped with a perfusion system to deliver the test hypo-osmotic solutions to the cells. As previously reported,[4] a hypo-osmotic stress provided by decreasing the osmolarity of the perfusion solution from 300 mOsm/L to 170 mOsm/L triggered a Ca^{2+} response (Figure 6A) in about 35% of cells expressing WT TMEM63B, while only a small fraction of control cells transfected with GCaMP6f responded (Figure 6B). Neuro2A cells expressing p.Val44Met showed reduced responsivity with respect to the WT-expressing cells. We also tested the response to weaker osmotic stresses that are more likely to be representative of physiological changes by shifting solution osmolarity from 300 mOsm/L down to 255 mOsm/L. The percentage of responsive cells

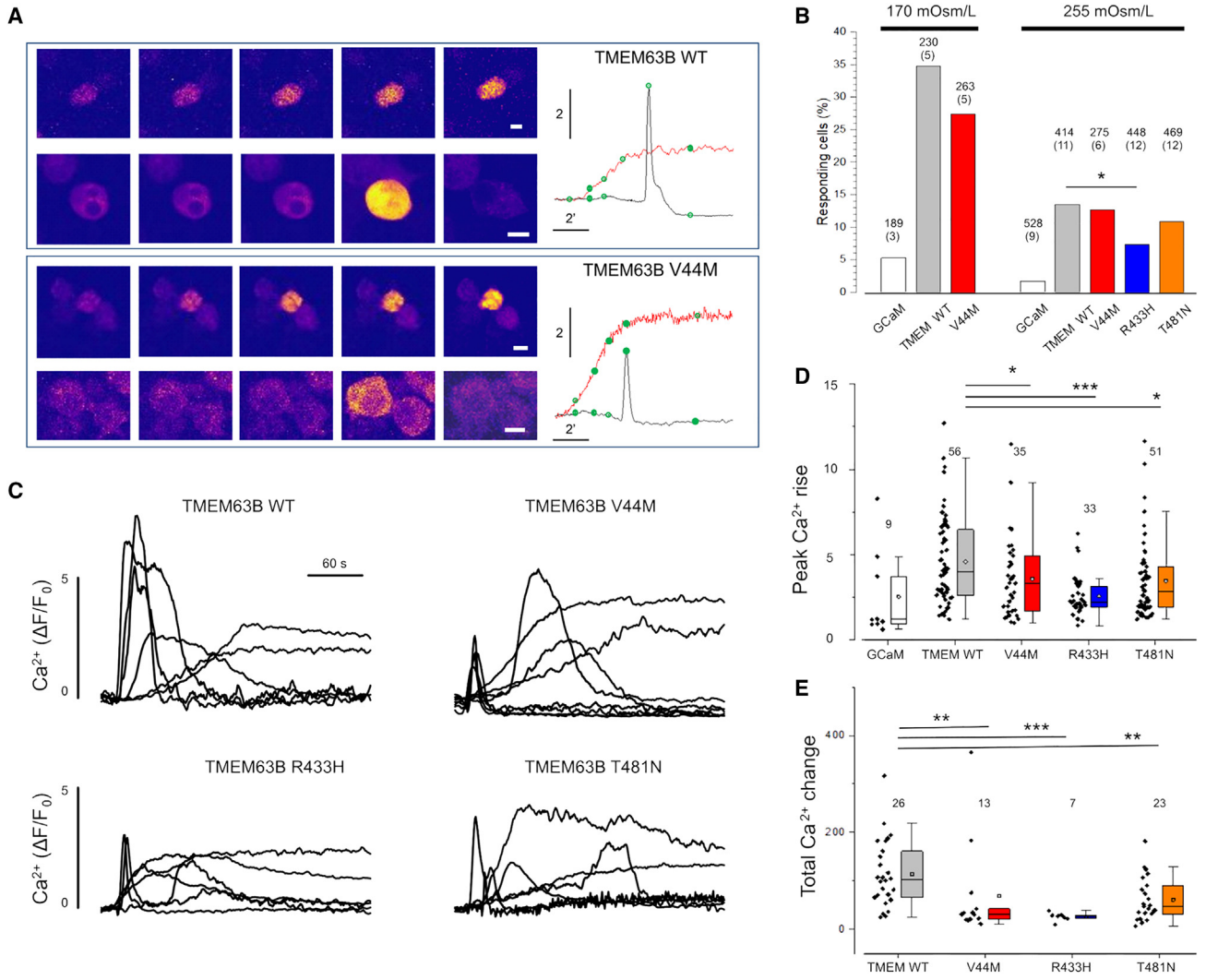

Figure 6. Mutations of TMEM63B impair the Ca^{2+} response to hypotonic stress

(A) Representative time-lapse sequence of Neuro2A cells co-transfected with WT and p.Val44Met TMEM63B after exposure to hypo-osmotic solution (170 mOsm/L). For each genotype, we show two cells characterized by transient or steady responses. The green dots on the traces indicate the timing of the images. Calibration bar is 10 μm in all images.

(B) Fraction of Neuro2A cells transfected with WT, p.Val44Met, p.Arg433His, or p.Thr481Asn TMEM63B presenting a Ca^{2+} response within 10 min from exposure to hypo-osmotic solutions. The number of analyzed cells is on top of each column, with the number of replicates in parentheses.

(C) Representative traces showing the change of fluorescence for several cells transfected with WT, p.Val44Met, p.Arg433His, or p.Thr481Asn TMEM63B.

(D) Cumulative results indicating the peak amplitude of the Ca^{2+} response to hypo-osmotic stimulus (255 mOsm/L). Numbers indicate the responding cells in each group. Total number of analyzed cells and replicates as indicated in (B).

(E) Integral of the Ca^{2+} change for the indicated experimental groups. In this analysis, we included only the cells that returned to baseline within 150 s from the transient onset. All mutants showed a drastically reduced response. Abbreviations and symbols: ***, $p < 0.001$; **, $p < 0.01$; *, $p < 0.05$ (chi-squared test); GCaM, control cells transfected with GCaMP6f empty vector. Data are expressed as box plots ranging from 25th percentile to 75th percentile, while the whiskers indicate the range of the outliers with a coefficient of 1.5.

decreased, and all the three mutants expressing cells showed a reduced responsivity score, which was significant for p.Arg433His (Figure 6B). The time course of representative responses plotted in Figures 6A and 6C shows a heterogeneous behavior of cells, ranging from transient Ca^{2+} pulses to sustained increments.

Given the role of Ca^{2+} in orchestrating the cell response to osmotic stress,[4] we next analyzed the amplitude and dynamics of the observed Ca^{2+} changes. Cells expressing the three variants showed smaller Ca^{2+} transient compared with those expressing WT TMEM63B. This is true when considering the maximal amplitude of the response (Figure 6D) and when considering the integral of the Ca^{2+} change computed for cells that returned to baseline within 150 s from the response onset (Figure 6E).

p.Val44Met and p.Gly580Cys cause lethal toxicity in *Drosophila*

About two-thirds of the vital genes in the *Drosophila* genome are involved in eye development, including genes required

for general cellular processes. For this reason, the fly eye provides an excellent experimental system to study the role of target genes in cellular function and development and in neurodevelopment/degeneration.[23] To evaluate the potential impact of selected variants on the eye morphology, we generated transgenic flies expressing the human *TMEM63B* gene. We designed transgenes for the WT *TMEM63B*, the recurrent p.Val44Met, and the p.Gly580Cys variants by using the GMR-Gal4 ectopic expression system, which is mostly expressed in the retina.[24] A schematic representation of the transgene construct is shown in Figure S9A. The Gal4-UAS system[25] induces *TMEM63B* expression by the binding of the yeast transcription factor Gal4 to the upstream activating sequence (UAS). The expression level of the Gal4/UAS system increases in a temperature-dependent manner[24] and can therefore be modulated by changing the fly-rearing temperatures. In WT *TMEM63B*-expressing flies, which were viable and reached the adult stage, we did not observe eye abnormalities (Figures S9B and S9C). However, when expressing the p.Val44Met and p.Gly580Cys *TMEM63B* transgenes, we did not obtain any adult fly as both variants caused early lethality. We could not obtain any adult fly even after reducing the expression level of the two transgenes to the minimum by lowering the rearing temperature down to 18°C. In adult flies expressing WT *TMEM63B* by *c739-Gal4*, we performed immunohistochemistry and observed dotted signals on the cell membrane (Figure S9D), thus demonstrating correct expression of the transgene in a neuronal cell type, Kenyon cells. We observed the same lethal phenotype by expressing the *TMEM63B* transgenes under either the *GMR-Gal4* or the *c739-Gal4* drivers, demonstrating that both variants caused lethal toxicity in *Drosophila*. Because the lack of either Kenyon cells or photoreceptors is not sufficient in itself to cause death in flies, we expect this phenotype to be caused by the expression of the p.Val44Met and p.Gly580Cys *TMEM63B* transgenes in other cell types indispensable during developmental stages.

Discussion

This series of 17 individuals with pathogenic heterozygous *de novo* variants of *TMEM63B* defines the phenotypic features of an autosomal dominant early-onset DEE syndrome. All individuals exhibited global developmental delay, moderate-to-profound intellectual disability, severe motor impairment, and severe epilepsy with onset from birth to 3 years. Three individuals had died prematurely, and those who had reached adolescent or adult age remained completely dependent. Most had central visual impairment and swallowing dysfunction requiring PEG insertion. Epilepsy was a prominent feature and was quite severe at onset, featuring recurrent episodes of status in some individuals, although a variable degree of seizure control was reported, with three individuals achieving seizure freedom on treatment. We noticed a common trajectory of the epilepsy phenotype, especially with the recurrent p.Val44Met variant, characterized by neonatal onset of apnoeic/focal seizures, evolving to epileptic spasms around the age of 4 to 6 months, and then continuing with focal, generalized seizures, or both. EEGs were consistent with an epileptic encephalopathy pattern at onset, including multifocal interictal epileptiform abnormalities and multiple seizure types in most. MRIs showed a consistent pattern of widespread or multiregional white matter abnormalities, with posterior periventricular predominance, dysmorphic lateral ventricles, thin corpus callosum, variably accompanied by global cerebellar atrophy (eight individuals), and areas of cortical atrophy (eight individuals). Overall, initial MRI findings in most individuals could be misdiagnosed as consequence of perinatal hypoxic-ischemic cerebral injury (see for example IDs 1, 3, 5, 7, 8, and 12–16). However, longitudinal neuroimaging with relatively long time intervals (up to 13 years) often revealed signs of progression, especially affecting the white matter and cerebellum. Over a clinical monitoring period up to ages 20 months to 30 years, three individuals died at ages 23 months, 9, and 12 years due to pneumonia. In the remaining 14 individuals, clinical findings were consistent with a DEE akin to cerebral palsy in most, with limited signs of progression in ten (IDs 1, 2, 5, 7–9, 13, and 15–17) and of a milder encephalopathy in four (IDs 3, 10, 11, and 14).

Overall, clinical and imaging findings are consistent with a progressive neurodegenerative clinical course and indicate, in most individuals, prenatal central nervous system impairment leading to onset of symptoms early after birth or within the first year of life. Hematological abnormalities might have contributed to brain damage. In 12 individuals, we found macrocytosis or signs of chronic hemolysis, often from birth, with a fluctuating course (Tables 1 and S2). Although such abnormalities were mostly not clinically significant or only caused jaundice in the neonatal period, in four individuals, the anemia was so severe it required periodic transfusions. In four of the individuals with anemia, MRI showed progressive thickening of the trabecular (spongy) bone of the skull (IDs 4, 8, and 13 in Figure 1 and individual 9, not shown), a finding often associated with severe hematological disorders.[26]

TMEM63B is evolutionarily conserved and highly intolerant to both LoF and missense variants in the general population. The International Mouse Phenotyping Consortium (IMPC, https://www.mousephenotype.org/) lists *Tmem63b* among the essential genes in database because its homozygous knockout causes pre-weaning lethality in the C57BL/6N strain.[27] Heterozygous *Tmem63b* mutant mice from the IMPC exhibit a neurodevelopmental phenotype and increased circulating bilirubin level, both consistent with observations in our individuals. No further significant hematological or sensorial abnormalities were observed in this mouse model, but susceptibility to epilepsy (e.g., by electroconvulsive threshold testing phenotypic assays) was not assessed. In a more vital

C57BL/6N-FVB/N mixed breed, surviving *Tmem63b* knockout mice developed progressive hearing loss.[4] Hearing impairment was described in 2/11 (18%) individuals who could be formally tested and in one more individual who was not tested. Because individuals with T*MEM63B*-associated DEE might be at increased risk of hearing impairment and this clinical problem is easily overlooked in the severely disabled, objective testing should be performed in this disorder.

Mendelian disease genes associated with autosomal dominant disorders are overrepresented among genes whose loss causes early development lethality (DL) in mice.[14] *TMEM63B* was prioritized among the potential candidates for human developmental disorders based on the overlap between genes that cause DL in mouse and those carrying *de novo* variants in large-scale human rare disease sequencing datasets.[14] Of five individuals with *de novo TMEM63B* variants included in the Deciphering Developmental Disorders (DDD[28]) and 100KGP[29] studies, with minimal phenotypic information, we could retrieve detailed clinical data in three, which we added to this series (IDs 4, 6, and 7; Table 1).

All ten variants were distributed in a TM domain conserved among osmosensitive calcium-permeable cation channels and affected residues under selective pressure in the general population, consistently with their predicted pathogenicity. None were a clear LoF/haploinsufficient variant (e.g., causing frameshift or premature stop codon). Heterozygous deletions including *TMEM63B* are rarely reported in the Database of Genomic Variants, where at least two individuals carry truncating deletions removing most of the gene (http://dgv.tcag.ca/; supporting variants nssv1153700 and nssv538990). Through our matchmaking initiative, we became aware of an individual with an unrelated phenotype and a homozygous p.Arg325* truncating variant of *TMEM63B* present in both healthy heterozygous parents (unpublished data). As we demonstrated in transfected Neuro2A, this variant abolished the expression of the mutated TMEM63B, in line with the predicted NMD.

These observations argue against haploinsufficiency being the obvious pathogenic mechanism in our cohort, as also supported by structural modeling and functional data. Structural modeling suggested mild changes in eight of ten of the variants without a disruptive effect on the protein structure. All ten variants affected TM helices, including TM4–TM8, constituting the channel pore, or TM1 and TM7, involved in sensing membrane tension,[2] and were predicted to cause minimal structural changes, such as disruption or creation of single salt bridges and changes in cavity volume. The predicted mutational consequences might therefore imply altered channel function, e.g., by stabilizing the pore opening or affecting ion permeability and selectivity. In line with this hypothesis, and as expected for variants sparing protein folding, none of the six variants we tested *in vitro* impaired protein localization in the plasma membrane.

The p.Val44Met was recurrent in seven individuals, and the remaining variants clustered across a ~270-residue TM region. Recurring mutations, as well as mutations with spatial clustering patterns, may exert their pathogenic effect through disease mechanisms other than LoF, such as gain of function (GoF) with enhanced activity or dominant-negative effects.[30,31]

We cannot exclude that variants in domains other than the TM helices or differently affecting the TMEM63B function, including LoF, might cause not-yet-described heterogeneous disorders.

In two independent *Drosophila* models, loss of *Tmem63* resulted in viable flies not exhibiting gross defects in coordination but lacking the ability to discriminate food texture or humidity.[32,33] In one of these models, the ectopic expression of the human *TMEM63B* gene in knockout flies rescued the defective phenotype in moisture attraction, demonstrating functional conservation of the two orthologs.[33] We thus decided to model the p.Val44Met and p.Gly580Cys variants in *Drosophila*. However, both p.Val44Met and p.Gly580Cys TMEM63B transgenes caused lethal toxicity in our models. In contrast, the phenotype of the WT *TMEM63B*-expressing flies was indistinguishable from the control animals. These observations suggest that the variants we tested cause a toxic GoF of TMEM63B rather than LoF.

Heterozygous variants of *TMEM63A* have been associated with developmental delay and hypomyelination.[6–8] Disease-associated missense variants are enriched at amino acid sites that are conserved across paralogs,[34] and differences in the clinical consequences of variants in paralogs may be due to different expression patterns and novel functions emerged with adaptive evolution.[35] When aligning protein sequence of and comparing variants positions in *TMEM63B* and *TMEM63A* (Figures 1A and S2), we found that the glycine 580 mutated to serine in ID 14 and to cysteine in ID 15 corresponds to the glycine 567 recurrently mutated to serine in *TMEM63A* in two unrelated individuals with transient hypomyelination.[6] The p.Gly580Ser affects a buried glycine in TM7. In the Arabidopsis AtOSCA1.1 channel, the corresponding glycine 528 is located in a bending of the TM6 helix.[2] Targeted mutagenesis of glycine 528 to alanine or proline reduces the pressure necessary to elicit a current, suggesting that channel activation might involve straightening of M6 around glycine 528 to relieve the blockage of the ion channel pore.[2] According to *in silico* prediction and structural modeling, we might expect that both variants of glycine 580 stabilize the structure of the pore.

Multiple expression datasets indicate a complementary expression pattern between *TMEM63A* and *TMEM63B*, with the first being mainly expressed in oligodendrocytes and the second strongly expressed in neurons and to a lesser extent in astrocytes and oligodendrocyte precursor cells (OPCs) (Figure S10; https://singlecell.broadinstitute.org; https://www.proteinatlas.org/). The six individuals reported to date with *TMEM63A* variants had follow-ups of

variable duration and exhibited phenotypes that were either similar to our individuals'[7,8] or milder in those whose white matter changes improved with age,[6] a phenomenon we did not observe.

For *in vitro* functional studies, we focused on the *TMEM63B* mRNA isoform most represented in the human cerebral cortex, the main generator of epileptogenic activity, and, in line with previous approaches,[4] we used Neuro2A cells to model six selected variants (p.Val44Met, p.Arg433His, p.Thr481Asn, p.Gly580Ser, p.Arg660Thr, and p.Phe697Leu). In physiologic isotonic conditions, the −80 mV step revealed inward leak currents in cells expressing mutants but not WT TMEM63B or control cells, indicating that the variants lead to a gain in conductance even in the absence of the hypo-osmotic stimulus gating the channel.

Under a hypo-osmotic challenge, we measured similar values of inward current amplitude in both mutant- and WT *TMEM63B*-expressing Neuro2A cells, suggesting that the variants do not alter the maximal channel conductance. However, the overall increase between currents measured in hypo-osmotic and isotonic conditions was larger in WT- than in mutant *TMEM63B*-expressing cells. Similarly, when we examined cells expressing the p.Val44Met, p.Arg433His, and p.Thr481Asn variants by calcium imaging, the Ca^{2+} transients generated under hypo-osmotic stimulation were smaller across the mutant channels compared with the WT. One possible explanation for these observations is that those three variants result in a selective reduction of the relative permeability for Ca^{2+} in favor of Na^{+}.

Inward cationic leak currents in neural cells expressing TMEM63B mutants may lead to altered neuronal excitability and/or impaired Ca^{2+} homeostasis. In C57BL/6N-FVB/N *Tmem63b* knockout mice, progressive hearing loss due to necroptosis of the outer hair cells (OHCs),[4] which face severe shape- and volume-changing conditions, was suggested to reflect an abnormal response to osmotic and mechanical stimuli, ultimately leading to cell death.[4] Brain shrinking with white matter changes, the main imaging finding in our series, might indicate neuronal loss, defective myelination, and possibly defective oligodendrocyte development. Clinical and imaging findings suggest that cell damage is already present at birth but further progresses postnatally. Already during prenatal life, several factors may determine osmotic challenges to the brain, including hydration changes, electrolyte imbalance, and mechanical stress. In a brain where neural cells are exceedingly vulnerable to even trivial volume changes and electrolytic imbalances, recurrent seizures may, in a vicious circle, make *TMEM63B*-defective neurons particularly susceptible to osmotic imbalance. During seizure activity, the extracellular environment surrounding axons and oligodendrocytes undergoes changes in volume and osmolarity,[36] and given the very small volume of the extracellular space surrounding myelinated axons, oligodendrocytes might be subjected to continuous changes in local osmolarity. Unfortunately, our understanding of the homeostasis of the extracellular space is still in its infancy.[37] In line with the above considerations, the epilepsy phenotype observed in our cohort is considerably more severe compared with other neurological conditions featuring structural damage of similar magnitude (i.e., cerebral palsy due to vascular injury).[38]

We hypothesize that the severe epileptic encephalopathy present in our individuals is caused by multiple converging factors including alteration of electrogenesis due to diffusely impaired ion currents and susceptibility to osmotic imbalance, resulting in structural brain damage, which can in turn be epileptogenic.

In 12 individuals, we also observed hematological abnormalities of variable severity, with signs of chronic hemolysis and myelodysplasia. In inherited hemolytic anemias, abnormally shaped RBCs may reflect disorders of cation permeability in the membrane, resulting in cellular over- or dehydration. Dehydrated hereditary stomatocytosis (DHSt), a rare congenital hemolytic anemia, is caused by dominant GoF mutations of *PIEZO1*, encoding for a stretch-activated ion channel.[39,40] In some individuals with DHSt, hematologic abnormalities are subtle,[39,40] as also seen in most of our individuals in whom they were revealed. In DHSt, *PIEZO1* mutations keep the channel in an open conformation with prolonged activity, resulting in Ca^{2+} influx and consequent K^{+} efflux though Ca-sensitive Gardos channels, decreasing intracellular osmolarity and causing dehydration of RBCs.[40,41] Although the role of *TMEM63B* in RBCs remains to be elucidated, it is known to be expressed in the RBC membrane (http://rbcc.hegelab.org/), such as *PIEZO1*, and might act similarly.

Erythrocytes are highly deformable cells. The intense mechanical solicitations they face when circulating through the brain microvasculature require highly effective mechanosensory feedback mechanisms. Under normal healthy conditions, deformability of their membrane allows RBCs to flow through vessels of diameter less than the cell diameter (7–8 μm), ensuring robust tissue perfusion and oxygen delivery.[42] This RBC feature is particularly critical in the brain microvascular network, where the diameter of cortical capillaries is around 4–5 μm.[43] RBCs also play an active role in stabilizing neurovascular flow dynamics, both by their physical properties[44] and by targeting the vascular endothelium with vasoactive molecules.[45] Chronic anemic changes and the physical vulnerability of *TMEM63B*-defective RBCs might contribute to white matter abnormalities, which often predominate in watershed vascular areas in the individuals reported here (Figure 1). Similar cerebrovascular complications are known to occur in individuals with hereditary hemolytic anemia.[46]

In conclusion, TMEM63B DEE represents a recognizable clinicopathological entity deriving from the dysfunctional behavior of a highly conserved stretch-activated ion channel. *TMEM63B* variants cause a gain in conductance with impaired Ca^{2+} homeostasis and are associated with neurodegenerative changes that start during prenatal brain development and slowly progress during postnatal development and adulthood, affecting the cerebral white and

gray matter and cerebellum. The clinical counterpart of such widespread anatomic abnormalities includes severe early-onset epilepsy, associated with moderate-to-profound intellectual disability and severe motor and cortical visual impairment. Although a clear genotype-phenotype correlation is not yet possible, the phenotype associated with the recurrent p.Val44Met variant is uniformly severe. Concomitant hematological changes make this a complex syndrome also featuring potentially life-threatening acute hemolytic episodes occurring without obvious triggers.

Consortia

The TMEM63B collaborators are Francesca Pochiero, Francesco Mari, Venkateswaran Ramesh, Valeria Capra, Margherita Mancardi, Boris Keren, Cyiril Mignot, Matteo Lulli, Kendall Parks, Helen Griffin, Melanie Brugger, Telethon Undiagnosed Diseases Program (TUDP) consortium, Vincenzo Nigro, Yuko Hirata, Reiko Koichihara, Borut Peterlin, Yuko Hirata, Ryuto Maki, and Yohei Nitta.

The members of the Genomics England Research Consortium are J.C. Ambrose, P. Arumugam, R. Bevers, M. Bleda, F. Boardman-Pretty, C.R. Boustred, H. Brittain, M.A. Brown, M.J. Caulfield, G.C. Chan, A. Giess, J. Griffin, A. Hamblin, S. Henderson, T.J.P. Hubbard, R. Jackson, L.J. Jones, D. Kasperaviciute, M. Kayikci, A. Kousathanas, L. Lahnstein, A. Lakey, S.E A. Leigh, I.U.S. Leong, F.J. Lopez, F. Maleady-Crowe, M. McEntagart, F. Minneci, J. Mitchell, L. Moutsianas, M. Mueller, N. Murugaesu, A.C. Need, P. O'Donovan, C.A. Odhams, C. Patch, D. Perez-Gil, M. B. Pereira, J. Pullinger, T. Rahim, A. Rendon, T. Rogers, K. Savage, K. Sawant, R.H. Scott, A. Siddiq, A. Sieghart, S.C. Smith, A. Sosinsky, A. Stuckey, M. Tanguy, A.L. Taylor Tavares, E.R.A. Thomas, S.R. Thompson, A. Tucci, M.J. Welland, E. Williams, K. Witkowska, S.M. Wood, and M. Zarowiecki.

Data and code availability

The data supporting the findings of this study are available within the article and/or its supplemental information. The exome datasets supporting this study have not been deposited in a public repository due to privacy and ethical/legal issues. *TMEM63B* genetic variants identified in our study have been submitted to DECIPHER (https://www.deciphergenomics.org; accession IDs 512417 and 512438–512452). Any additional raw data are available on request from the corresponding author.

Supplemental information

Supplemental information can be found online at https://doi.org/10.1016/j.ajhg.2023.06.008.

Acknowledgments

We are grateful to all the research subjects and family members for their participation in this study. This work was generated within the European Reference Networks EpiCARE and ITHACA. This work was supported by grants to R.G. from the Tuscany Region Call for Health 2018 (grant DECODE-EE) and Fondazione Cassa di Risparmio di Firenze (Human Brain Optical Mapping Project). Support to E.A. in sequencing and analysis was provided by the Broad Institute of MIT and Harvard Center for Mendelian Genomics (Broad CMG) and by the National Human Genome Research Institute, the National Eye Institute, and the National Heart, Lung, and Blood Institute grant UM1 HG008900 and in part by National Human Genome Research Institute grant R01 HG009141. A.T. was supported by Fondazione Telethon, Telethon Undiagnosed Diseases Program (grant GSP15001). N.M. received support from the Japan Agency for Medical Research and Development (AMED) under grant numbers JP22ek0109486, JP22ek0109549, and JP22ek0109493 and the Takeda Science Foundation. T.R. was supported by the Australian NHMRC Centre for Research Excellence in Neurocognition (1117394).

Author contributions

R.G. designed the research study, acquired and analyzed clinical and genetic data, and drafted the manuscript; A.V. participated in designing the research study, analyzed genetic data, and drafted the manuscript; S.B. acquired and analyzed clinical data and participated in drafting the manuscript; C.P. analyzed functional data, performed statistical analysis, and participated in drafting the manuscript; G.M.R. participated in designing functional studies in transfected cells, analyzed calcium imaging data, and performed statistical analysis; V.C. participated in designing functional studies and in genetic and protein structural data analysis; A.M., G.M., R.P., and S.G. performed experimental analyses in transfected cells; K.H. and H.O. participated in protein structural data analysis; A.D., C.v.S., E.V., G.B., J.J.v.d.S., M.K., M.P.M., M. Sakamoto, N.M., R.B., R.R., S.H., T.B., and T.R. acquired clinical and genetic data; E.A., E.K.B., J.T., K.W., M. Scala, R.K., S.M., and S.V. acquired clinical data; A.T., D.M., D.S., E.H.S., K.M., K.v.G., M.J.V.H., P.C., and T.C. acquired genetic data; A.S. and T.S. produced and analyzed *Drosophila* models.

Declaration of interests

The authors have declared that no conflict of interest exists.

Received: November 28, 2022
Accepted: June 13, 2023
Published: July 7, 2023

References

1. Murthy, S.E., Dubin, A.E., Whitwam, T., Jojoa-Cruz, S., Cahalan, S.M., Mousavi, S.A.R., Ward, A.B., and Patapoutian, A. (2018). OSCA/TMEM63 are an evolutionarily conserved family of mechanically activated ion channels. Elife *7*, e41844. https://doi.org/10.7554/eLife.41844.
2. Zhang, M., Wang, D., Kang, Y., Wu, J.-X., Yao, F., Pan, C., Yan, Z., Song, C., and Chen, L. (2018). Structure of the mechanosensitive OSCA channels. Nat. Struct. Mol. Biol. *25*, 850–858. https://doi.org/10.1038/s41594-018-0117-6.
3. Yuan, F., Yang, H., Xue, Y., Kong, D., Ye, R., Li, C., Zhang, J., Theprungsirikul, L., Shrift, T., Krichilsky, B., et al. (2014). OSCA1 mediates osmotic-stress-evoked Ca2+ increases vital

for osmosensing in Arabidopsis. Nature *514*, 367–371. https://doi.org/10.1038/nature13593.

4. Du, H., Ye, C., Wu, D., Zang, Y.Y., Zhang, L., Chen, C., He, X.Y., Yang, J.J., Hu, P., Xu, Z., et al. (2020). The Cation Channel TMEM63B Is an Osmosensor Required for Hearing. Cell Rep. *31*, 107596. https://doi.org/10.1016/j.celrep.2020.107596.
5. Lang, F., Busch, G.L., Ritter, M., Völkl, H., Waldegger, S., Gulbins, E., and Häussinger, D. (1998). Functional significance of cell volume regulatory mechanisms. Physiol. Rev. *78*, 247–306. https://doi.org/10.1152/physrev.1998.78.1.247.
6. Yan, H., Helman, G., Murthy, S.E., Ji, H., Crawford, J., Kubisiak, T., Bent, S.J., Xiao, J., Taft, R.J., Coombs, A., et al. (2019). Heterozygous Variants in the Mechanosensitive Ion Channel TMEM63A Result in Transient Hypomyelination during Infancy. Am. J. Hum. Genet. *105*, 996–1004. https://doi.org/10.1016/j.ajhg.2019.09.011.
7. Fukumura, S., Hiraide, T., Yamamoto, A., Tsuchida, K., Aoto, K., Nakashima, M., and Saitsu, H. (2022). A novel de novo TMEM63A variant in a patient with severe hypomyelination and global developmental delay. Brain Dev. *44*, 178–183. https://doi.org/10.1016/j.braindev.2021.09.006.
8. Tonduti, D., Mura, E., Masnada, S., Bertini, E., Aiello, C., Zini, D., Parmeggiani, L., Cantalupo, G., Talenti, G., Veggiotti, P., et al. (2021). Spinal cord involvement and paroxysmal events in "Infantile Onset Transient Hypomyelination" due to TMEM63A mutation. J. Hum. Genet. *66*, 1035–1037. https://doi.org/10.1038/s10038-021-00921-1.
9. Tábara, L.C., Al-Salmi, F., Maroofian, R., Al-Futaisi, A.M., Al-Murshedi, F., Kennedy, J., Day, J.O., Courtin, T., Al-Khayat, A., Galedari, H., et al. (2022). TMEM63C mutations cause mitochondrial morphology defects and underlie hereditary spastic paraplegia. Brain *145*, 3095–3107. https://doi.org/10.1093/brain/awac123.
10. Wu, D., Zang, Y.Y., Shi, Y.Y., Ye, C., Cai, W.M., Tang, X.H., Zhao, L., Liu, Y., Gan, Z., Chen, G.Q., et al. (2020). Distant coupling between RNA editing and alternative splicing of the osmosensitive cation channel tmem63b. J. Biol. Chem. *295*, 18199–18212. https://doi.org/10.1074/jbc.RA120.016049.
11. Vetro, A., Nielsen, H.N., Holm, R., Hevner, R.F., Parrini, E., Powis, Z., Møller, R.S., Bellan, C., Simonati, A., Lesca, G., et al. (2021). ATP1A2-and ATP1A3-associated early profound epileptic encephalopathy and polymicrogyria. Brain *144*, 1435–1450. https://doi.org/10.1093/brain/awab052.
12. Sobreira, N., Schiettecatte, F., Valle, D., and Hamosh, A. (2015). GeneMatcher: a matching tool for connecting investigators with an interest in the same gene. Hum. Mutat. *36*, 928–930. https://doi.org/10.1002/humu.22844.
13. Scheffer, I.E., Berkovic, S., Capovilla, G., Connolly, M.B., French, J., Guilhoto, L., Hirsch, E., Jain, S., Mathern, G.W., Moshé, S.L., et al. (2017). ILAE classification of the epilepsies: Position paper of the ILAE Commission for Classification and Terminology. Epilepsia *58*, 512–521. https://doi.org/10.1111/epi.13709.
14. Cacheiro, P., Muñoz-Fuentes, V., Murray, S.A., Dickinson, M.E., Bucan, M., Nutter, L.M.J., Peterson, K.A., Haselimashhadi, H., Flenniken, A.M., Morgan, H., et al. (2020). Human and mouse essentiality screens as a resource for disease gene discovery. Nat. Commun. *11*, 655. https://doi.org/10.1038/s41467-020-14284-2.
15. Wiel, L., Baakman, C., Gilissen, D., Veltman, J.A., Vriend, G., and Gilissen, C. (2019). MetaDome: Pathogenicity analysis of genetic variants through aggregation of homologous human protein domains. Hum. Mutat. *40*, 1030–1038. https://doi.org/10.1002/humu.23798.
16. Hou, C., Tian, W., Kleist, T., He, K., Garcia, V., Bai, F., Hao, Y., Luan, S., and Li, L. (2014). DUF221 proteins are a family of osmosensitive calcium-permeable cation channels conserved across eukaryotes. Cell Res. *24*, 632–635. https://doi.org/10.1038/cr.2014.14.
17. Maity, K., Heumann, J.M., McGrath, A.P., Kopcho, N.J., Hsu, P.K., Lee, C.W., Mapes, J.H., Garza, D., Krishnan, S., Morgan, G.P., et al. (2019). Cryo-EM structure of OSCA1.2 from Oryza sativa elucidates the mechanical basis of potential membrane hyperosmolality gating. Proc. Natl. Acad. Sci. USA *116*, 14309–14318. https://doi.org/10.1073/pnas.1900774116.
18. Liu, X., Wang, J., and Sun, L. (2018). Structure of the hyperosmolality-gated calcium-permeable channel OSCA1.2. Nat. Commun. *9*, 5060. https://doi.org/10.1038/s41467-018-07564-5.
19. Ittisoponpisan, S., Islam, S.A., Khanna, T., Alhuzimi, E., David, A., and Sternberg, M.J.E. (2019). Can Predicted Protein 3D Structures Provide Reliable Insights into whether Missense Variants Are Disease Associated? J. Mol. Biol. *431*, 2197–2212. https://doi.org/10.1016/j.jmb.2019.04.009.
20. Guo, R., Cang, Z., Yao, J., Kim, M., Deans, E., Wei, G., Kang, S.G., and Hong, H. (2020). Structural cavities are critical to balancing stability and activity of a membrane-integral enzyme. Proc. Natl. Acad. Sci. USA *117*, 22146–22156. https://doi.org/10.1073/pnas.1917770117.
21. Marques, M.C., Albuquerque, I.S., Vaz, S.H., and Bernardes, G.J.L. (2019). Overexpression of Osmosensitive Ca2+-Permeable Channel TMEM63B Promotes Migration in HEK293T Cells. Biochemistry *58*, 2861–2866. https://doi.org/10.1021/acs.biochem.9b00224.
22. Zhao, X., Yan, X., Liu, Y., Zhang, P., and Ni, X. (2016). Co-expression of mouse TMEM63A, TMEM63B and TMEM63C confers hyperosmolarity activated ion currents in HEK293 cells. Cell Biochem. Funct. *34*, 238–241. https://doi.org/10.1002/cbf.3185.
23. Iyer, J., Wang, Q., Le, T., Pizzo, L., Grönke, S., Ambegaokar, S.S., Imai, Y., Srivastava, A., Troisí, B.L., Mardon, G., et al. (2016). Quantitative Assessment of Eye Phenotypes for Functional Genetic Studies Using *Drosophila melanogaster*. G3 *6*, 1427–1437. https://doi.org/10.1534/g3.116.027060.
24. Kramer, J.M., and Staveley, B.E. (2003). GAL4 causes developmental defects and apoptosis when expressed in the developing eye of Drosophila melanogaster. Genet. Mol. Res. *2*, 43–47.
25. Brand, A.H., and Perrimon, N. (1993). Targeted gene expression as a means of altering cell fates and generating dominant phenotypes. Development *118*, 401–415. https://doi.org/10.1242/dev.118.2.401.
26. Andreu-Arasa, V.C., Chapman, M.N., Kuno, H., Fujita, A., and Sakai, O. (2018). Craniofacial manifestations of systemic disorders: CT and MR imaging findings and imaging approach. Radiographics *38*, 890–911. https://doi.org/10.1148/rg.2018170145.
27. Dickinson, M.E., Flenniken, A.M., Ji, X., Teboul, L., Wong, M.D., White, J.K., Meehan, T.F., Weninger, W.J., Westerberg, H., Adissu, H., et al. (2016). High-throughput discovery of novel developmental phenotypes. Nature *537*, 508–514. https://doi.org/10.1038/nature19356.
28. Firth, H.V., Richards, S.M., Bevan, A.P., Clayton, S., Corpas, M., Rajan, D., Van Vooren, S., Moreau, Y., Pettett, R.M., and Carter, N.P. (2009). DECIPHER: Database of Chromosomal Imbalance and Phenotype in Humans Using Ensembl

Resources. Am. J. Hum. Genet. *84*, 524–533. https://doi.org/10.1016/j.ajhg.2009.03.010.
29. Turnbull, C., Scott, R.H., Thomas, E., Jones, L., Murugaesu, N., Pretty, F.B., Halai, D., Baple, E., Craig, C., Hamblin, A., et al. (2018). The 100 000 Genomes Project: Bringing whole genome sequencing to the NHS. BMJ *361*, k1687. https://doi.org/10.1136/bmj.k1687.
30. Lelieveld, S.H., Wiel, L., Venselaar, H., Pfundt, R., Vriend, G., Veltman, J.A., Brunner, H.G., Vissers, L.E.L.M., and Gilissen, C. (2017). Spatial Clustering of de Novo Missense Mutations Identifies Candidate Neurodevelopmental Disorder-Associated Genes. Am. J. Hum. Genet. *101*, 478–484. https://doi.org/10.1016/j.ajhg.2017.08.004.
31. Wilkie, A.O. (1994). The molecular basis of genetic dominance. J. Med. Genet. *31*, 89–98. https://doi.org/10.1136/jmg.31.2.89.
32. Li, Q., and Montell, C. (2021). Mechanism for food texture preference based on grittiness. Curr. Biol. *31*, 1850–1861.e6. https://doi.org/10.1016/j.cub.2021.02.007.
33. Li, S., Li, B., Gao, L., Wang, J., and Yan, Z. (2022). Humidity response in Drosophila olfactory sensory neurons requires the mechanosensitive channel TMEM63. Nat. Commun. *13*, 3814. https://doi.org/10.1038/s41467-022-31253-z.
34. Lal, D., May, P., Perez-Palma, E., Samocha, K.E., Kosmicki, J.A., Robinson, E.B., Møller, R.S., Krause, R., Nürnberg, P., Weckhuysen, S., et al. (2020). Gene family information facilitates variant interpretation and identification of disease-associated genes in neurodevelopmental disorders. Genome Med. *12*, 28. https://doi.org/10.1186/s13073-020-00725-6.
35. Guschanski, K., Warnefors, M., and Kaessmann, H. (2017). The evolution of duplicate gene expression in mammalian organs. Genome Res. *27*, 1461–1474. https://doi.org/10.1101/gr.215566.116.
36. Lux, H.D., Heinemann, U., and Dietzel, I. (1986). Ionic changes and alterations in the size of the extracellular space during epileptic activity. Adv. Neurol. *44*, 619–639.
37. Sætra, M.J., Einevoll, G.T., and Halnes, G. (2021). An electrodiffusive neuron-extracellular-glia model for exploring the genesis of slow potentials in the brain. PLoS Comput. Biol. *17*, e1008143. https://doi.org/10.1371/journal.pcbi.1008143.
38. Cooper, M.S., Mackay, M.T., Dagia, C., Fahey, M.C., Howell, K.B., Reddihough, D., Reid, S., and Harvey, A.S. (2023). Epilepsy syndromes in cerebral palsy: varied, evolving and mostly self-limited. Brain *146*, 587–599. https://doi.org/10.1093/brain/awac274.
39. Andolfo, I., Alper, S.L., De Franceschi, L., Auriemma, C., Russo, R., De Falco, L., Vallefuoco, F., Esposito, M.R., Vandorpe, D.H., Shmukler, B.E., et al. (2013). Multiple clinical forms of dehydrated hereditary stomatocytosis arise from mutations in PIEZO1. Blood *121*, 3925–3935. https://doi.org/10.1182/blood-2013-02-482489.
40. Albuisson, J., Murthy, S.E., Bandell, M., Coste, B., Louis-Dit-Picard, H., Mathur, J., Fénéant-Thibault, M., Tertian, G., De Jaureguiberry, J.P., Syfuss, P.Y., et al. (2013). Dehydrated hereditary stomatocytosis linked to gain-of-function mutations in mechanically activated PIEZO1 ion channels. Nat. Commun. *4*, 1884. https://doi.org/10.1038/ncomms2899.
41. Caulier, A., and Garçon, L. (2022). PIEZO1, sensing the touch during erythropoiesis. Curr. Opin. Hematol. *29*, 112–118. https://doi.org/10.1097/MOH.0000000000000706.
42. Ebrahimi, S., and Bagchi, P. (2022). A computational study of red blood cell deformability effect on hemodynamic alteration in capillary vessel networks. Sci. Rep. *12*, 4304. https://doi.org/10.1038/s41598-022-08357-z.
43. Schmid, F., Barrett, M.J.P., Jenny, P., and Weber, B. (2019). Vascular density and distribution in neocortex. Neuroimage *197*, 792–805. https://doi.org/10.1016/j.neuroimage.2017.06.046.
44. Schmid, F., Barrett, M.J.P., Obrist, D., Weber, B., and Jenny, P. (2019). Red blood cells stabilize flow in brain microvascular networks. PLoS Comput. Biol. *15*, e1007231. https://doi.org/10.1371/journal.pcbi.1007231.
45. Richardson, K.J., Kuck, L., and Simmonds, M.J. (2020). Beyond oxygen transport: active role of erythrocytes in the regulation of blood flow. Am. J. Physiol. Heart Circ. Physiol. *319*, H866–H872. https://doi.org/10.1152/AJPHEART.00441.2020.
46. Patel, R., Sabat, S., and Kanekar, S. (2016). Imaging Manifestations of Neurologic Complications in Anemia. Hematol. Oncol. Clin. North Am. *30*. *30*, 733–756. https://doi.org/10.1016/j.hoc.2016.03.002.

The American Journal of Human Genetics, Volume *110*

Supplemental information

Stretch-activated ion channel TMEM63B associates with developmental and epileptic encephalopathies and progressive neurodegeneration

Annalisa Vetro, Cristiana Pelorosso, Simona Balestrini, Alessio Masi, Sophie Hambleton, Emanuela Argilli, Valerio Conti, Simone Giubbolini, Rebekah Barrick, Gaber Bergant, Karin Writzl, Emilia K. Bijlsma, Theresa Brunet, Pilar Cacheiro, Davide Mei, Anita Devlin, Mariëtte J.V. Hoffer, Keren Machol, Guido Mannaioni, Masamune Sakamoto, Manoj P. Menezes, Thomas Courtin, Elliott Sherr, Riccardo Parra, Ruth Richardson, Tony Roscioli, Marcello Scala, Celina von Stülpnagel, Damian Smedley, TMEM63B collaborators, The Genomics England Research Consortium, Annalaura Torella, Jun Tohyama, Reiko Koichihara, Keisuke Hamada, Kazuhiro Ogata, Takashi Suzuki, Atsushi Sugie, Jasper J. van der Smagt, Koen van Gassen, Stephanie Valence, Emma Vittery, Stephen Malone, Mitsuhiro Kato, Naomichi Matsumoto, Gian Michele Ratto, and Renzo Guerrini

Supplemental information

Sections:

Supplemental Materials and Methods

MRI investigations

All individuals underwent standard brain magnetic resonance imaging (MRI) as part of their routine clinical care. Ten out of 17 individuals were imaged at least twice. Data were acquired using 1.5-T or 3-T systems, with T1-weighted, T2-weighted, and fluid attenuated inversion recovery (FLAIR) sequences in axial, sagittal, and coronal planes at the respective centers.

Genetic investigations

We performed whole exome (WES, IDs 1-3, 5, and 8-17) and genome (WGS, IDs 4 and 6) sequencing using standard procedures on DNA extracted from peripheral blood. In all but IDs 7 and 10, whose DNA was sequenced as singleton, we used a patient-parent trio sequencing strategy. We prepared DNA libraries by different kits according to manufacturers' instructions and performed paired-end sequencing on Illumina sequencers (Illumina, San Diego, CA, USA). We aligned sequencing reads to the human reference genome build GRCh37/hg19 by the Burrows-Wheeler Alignment (BWA-MEM) software package[1] and followed the Genome Analysis Toolkit Best Practices workflow[2] for variant calling. Detailed sequencing and variant annotation methods for each individual are provided as a reference to previous publications in the Supplementary Table 4. For variant analysis, we focused on exonic/splice-site single-nucleotide variants (SNVs) and coding insertions/deletions (InDels) with minor allele frequency (MAF) lower than 0.01 in the GnomAD v2.1 (http://gnomad.broadinstitute.org/)[3] or TOPMed (https://bravo.sph.umich.edu/freeze3a/hg19/) datasets. We excluded population-specific variants by interrogating our internal database (singleton WES data from approximately 2000 individuals with DEE). We evaluated the potential impact of SNVs and InDels by the pre-computed genomic variants score from dbNSFP[4] and by the evolutionary conservation scores.[5,6] After filtering and interpretation, we proceeded to validation of the *TMEM63B* variants by Sanger sequencing (primers and conditions available on request). We followed the nomenclature guidelines of the Human Genome Variation Society (HGVS, http://www.hgvs.org/mutnomen) and referred to the NM_018426.3 reference transcript.

We evaluated *TMEM63B* gene-level constraint scores according to GnomAD[3] and the region-level constraint scores according to the Metadome and MTR tools.[7,8]

Homology modelling and structural analysis

To evaluate the evolutionary conservation of the mutated residues, we obtained the protein sequence of human TMEM63B, its paralogues TMEM63A and TMEM63C, and orthologues in five different vertebrate species (*Pan troglodytes, Sus scrofa, Mus musculus, Gallus gallus, Danio rerio*) from the NCBI Protein Database,[9] and aligned them using Clustal Omega.[10] As the protein crystal structure of TMEM63B has not been determined, we used the protein homology recognition engine Phyre2[11] to predict and analyse the protein structure. For structural modelling, we referred to the NP_060896.1 human TMEM63B protein sequence using the Phyre2 'intensive mode' prediction option. To further analyse possible effects of the recurrent p.Val44Met, we calculated the free energy change due to this substitution by the FoldX software[12,13] using a TMEM63B structural model predicted by AlphaFold2.[14] We also generated a tridimensional model incorporating evolutionary sequence conservation with the ConSurf webserver[15] with default parameters. We used the Missense3D tool[16] to predict possible structural changes introduced by the missense substitutions. To graphically represent the variants identified in our individuals on the homology-predicted protein model we used the UCSF Chimera Visualization System.[17]

RNA reverse transcription and cDNA analyses

We reverse-transcribed total RNA from healthy adult human cerebral cortex (BioChain, Newark, USA) into cDNA using the High-Capacity RNA-to-cDNA Kit (Applied Biosystems, Waltham, USA). We performed polymerase chain reaction (PCR) on the cDNA using the FastStart Taq DNA Polymerase (Roche, Basel, Switzerland) and *TMEM63B* primers designed with the Primer3 Plus software (https://www.bioinformatics.nl/cgi-bin/primer3plus/primer3plus.cgi) using the NM_018426.3 transcript as template. Primers and RT-PCR conditions are available upon request.

To characterise the alternative splicing of exon 4 in the *TMEM63B*, we amplified the cDNA region spanning the exon 4 (exons 3-8) and analysed the PCR product by agarose gel electrophoresis. We acquired the gel images by ChemiDoc Imaging System (Bio-Rad, Hercules, USA) and quantified the two cDNA bands we resolved by ImageJ software (National Institutes of Health, USA). We quantified the expression level of the two isoforms as the ratio of integrated densities of the two bands to the total. We extracted the cDNAs from

excised gel bands (Macherey-Nagel, Düren, Germany), sequenced them and analysed the electropherograms using the SnapGene software (https://www.snapgene.com/) to confirm that they corresponded to the two *TMEM63B* isoforms with (herein referred to as "long" isoform) or without (herein referred to as "short" isoform) exon 4. As an orthogonal method to confirm the relative expression level of both isoforms, we also cloned the PCR product in TOPO TA cloning (Invitrogen, Waltham, USA) and used Sanger Sequencing to determine the number of colonies containing the long or the short isoform.

To characterise the Q/R editing at exon 20 in the *TMEM63B*, we amplified the cDNA region including exon 20 in both isoforms. To quantify the editing occurrence in both isoforms, we cloned the PCR products in TOPO TA cloning and counted the number of colonies containing the editing.

TMEM63B constructs

We designed wild type (WT) and mutant (p.Arg325*, p.Val44Met, p.Arg433His, p.Thr481Asn, p.Gly580Ser, p.Arg660Thr, and p.Phe697Leu) human *TMEM63B* cDNAs corresponding to the most represented isoform in the human cerebral cortex (short not edited), with the hemagglutinin (HA) tag sequence (AGCGTAATCTGGAACATCGTATGGGTA) at the 5' end. We obtained *TMEM63B* cDNAs and cloned them into the pGP-CMV-GCaMP6f vector (Plasmid #40755, Addgene, Watertown, USA),[18] so that the cDNA is fused to the N-terminus of GCaMP6f via a P2A linker forming a tandem expression system (TMEM63B-P2A-GCaMP6f) (Genescript, Piscataway, USA). The correct orientation and sequence of the cDNAs were checked by Sanger sequencing by Genescript.

Cell culture and transfection

We maintained Neuro2A mouse neuroblastoma cells at 37°C in a humidified 5% CO_2 incubator in Dulbecco's Modified Eagle Medium (Invitrogen, Waltham, USA) supplemented with 10% foetal bovine serum (FBS) and 2 mM L-glutamine. For the electrophysiology experiments, we plated the cells onto 13 mm square glass poly-L-lysine coated coverslips. The cells used in the Ca-imaging experiments were plated on WillCo Wells dishes HBST-3512 (WillCo Wells B.V., Amsterdam, The Netherlands). We transfected Neuro2A cells using Lipofectamine 2000 (Invitrogen) according to manufacturer's instruction.

Immunocytochemistry and confocal microscopy

Forty-eight hours post transfection, we fixed Neuro2A cells in 4% paraformaldehyde in phosphate-buffered saline (PBS) for 15 minutes at room temperature, blocked with 10% normal goat serum and 0.1% bovine serum albumin (BSA) in PBS for one hour at room temperature and incubated in 0.1% BSA in PBS overnight at 4°C with the primary anti-HA tag antibody (1:500, #2367, Cell Signaling Technology, Inc., Danvers, USA). After washing in PBS, we incubated the cells in 0.1% BSA in PBS for one hour at room temperature with the secondary Alexa Fluor 555 antibody (1:500, #A21424, Thermo Fisher Scientific, Waltham, USA). We washed the cells in PBS and mounted coverslips with ProLong Gold Antifade Mountant with DAPI (#P36935, Thermo-Fisher Scientific). We acquired images of 100 x 100 µm area using a laser scanning confocal microscope (SP5, Leica, Wetzlar, Germany) and analysed data with ImageJ software (National Institutes of Health, Bethesda, USA).

In *Drosophila*, we performed immunohistochemistry and sample preparation as described previously.[19] Briefly, we dissected the adult fly brains in PBS, fixed them in 4% formaldehyde (Electron Microscopy Sciences, USA), and incubated the samples with mouse anti-myc (4A6; 1:5000; Merck KGaA, Darmstadt, Germany) and secondary anti-mouse Alexa Fluor 568 (1:400; Thermo Fisher Scientific). We acquired images using a FV3000 confocal microscope (Olympus, Tokyo, Japan), and processed and analysed them using IMARIS 9.6.0 (Bitplane, Zurich, Switzerland).

Electrophysiology

Forty-eight hours post transfection, we recorded Neuro2A cells by whole-cell patch clamp. Recording pipettes were obtained from borosilicate capillaries (Harvard Apparatus, Holliston, USA) with a Narishige vertical puller (Narishige, Tokyo, Japan) and back-filled with a solution containing (in mM) 80 K-gluconate, 10 HEPES, 130 Mannitol (pH 7.4 with KOH, 300 mOsm/L), resulting in a bath resistance of 8-10 MΩ. We initially perfused cells with an isotonic extracellular solution containing (in mM): 80 Na-gluconate, 1 Ca-gluconate, 10 HEPES, 130 Mannitol (pH 7.4 with NaOH, 300 mOsm/L) at room temperature and with a flow rate of approximately 1 ml/min. The hypo-osmotic extracellular solution contained (in mM): 80 Na-gluconate, 1 Ca-gluconate and 10 HEPES (pH 7.4 with NaOH, 170 mOsm/L). The osmolarity of the solutions used in both patch clamp and calcium imaging experiments was measured by an osmometer (OSMOMAT 030,

Gonotec Gmbh, Berlin, Germany). Solutions were exchanged with an eight-line valve switcher (Hamilton Company, Reno, USA). We stimulated the cells with a voltage clamp protocol consisting of a 40 ms negative step to -80 mV, followed by a 100 ms ramp stimulus to +80 mV, imposed every 10 seconds. Holding potential was 0 mV. Signals were sampled at 10 kHz and low pass filtered at 3 kHz with an Axon Multiclamp 700B (Molecular Devices, Sunnyvale, USA). We performed data analysis offline with Clampfit 10 (Molecular Devices) and GraphPad 8.0 software (GraphPad, San Diego, USA).

Calcium imaging

Forty-eight hours post transfection, we acquired cells imaging with a ZEISS LSM800 Airyscan inverted microscope (ZEISS, Jena, Germany) at a resolution of 512x512 pixels (objective ZEISS ECPlan-NEOFLUAR 20x) with the standard settings for excitation and acquisition of Fluorescein (excitation 488nm, emission >500nm) at 0.5 Hz frequency for 600 seconds. During imaging, cells were exposed to solutions of variable osmolarity by perfusing the imaging chamber with peristaltic pumps (flux 1ml/min). The hypo-osmotic solution contained (mM): 65 NaCl, 5 KCl, 1 $CaCl_2$ 2, 1 $MgCl_2$ 2, 10 HEPES, pH=7.4, adjusted with NaOH. We prepared the isotonic solution adding mannitol to the hypo-osmotic solution to a final concentration of mannitol 130 mM without changing other ion concentrations.

Analysis of calcium imaging data

We analysed the acquired images with Fiji ImageJ software. For each field of acquisition, we generated an average projection, and we selected the cells which florescence was in the upper 95 percentile to exclude autofluorescent cells. We then analysed the selected cells by computing the fractional change of fluorescence defined as:

$$\Delta F(t) = \frac{F(t) - F_0}{F_0}$$

where F_0 indicates the baseline fluorescence computed as the average of the first 20 frames of the sequence. Cells were considered responsive when they presented changes of fluorescence larger than 50% of the baseline level.

Statistical analysis

We used the GraphPad 8.0 software for statistical analyses. We assessed the normal distribution of experimental data using the D'Agostino-Pearson normality test. We analysed data with normal distribution with One-way ANOVA followed by Tukey's multiple comparison test, while for non-normally distributed data we used the unpaired Mann-Whitney U test or Kruskal-Wallis test followed by Dunn's multiple comparison test. We set significance level at $p<0.05$ and expressed data as mean ± standard error of the mean (SEM).

For statistical analysis of calcium imaging, we used the Origin 2019b package (OriginLab, Massachusetts, USA). Hypotheses were tested with Mann-Whitney non-parametric tests. We considered results to be significant for $p<0.05$.

Drosophila strains and generation of the transgenic lines expressing human *TMEM63B* WT, p.Val44Met, and p.Gly580Cys

Flies were maintained at 25°C on standard fly food. *GMR-Gal4* (#1104) and *c739-Gal4* with *UAS-CD8GFP* (#64305) were obtained from the BDRC (Bloomington, Indiana, USA). *40D-UAS* (#60101) for control experiments was purchased from VDRC (Vienna, Austria). To express human TMEM63B WT, p.Val44Met, and p.Gly580Cys, tagged with Myc at C terminal of the protein, the cDNAs were inserted into pJFRC81-10XUAS-IVS-Syn21-GFP-p10 (ID36432, Addgene, Massachusetts, USA) (Vectorbuilder Inc., Yokohama, Japan). We used the phiC31 integrase system[20] to insert the transgenes in the same position of the fly genome and exclude potential positional effects on gene expression. These vectors were inserted into the *aTTP40* landing site (WellGenetics, Taipei, Taiwan). As the expression level of the Gal4/UAS system increases in a temperature-dependent manner,[21] the transgenic flies were reared at different temperatures (18°, 20°, 25° and 29°C), to modulate the expression of the transgene.

Eye imaging with bright-field microscopy and the quantification of morphological defects in the retina

TMEM63B WT and each the two variants p.Val44Met and p.Gly580Cys were expressed by the *GMR-Gal4* driver and reared at 20°C. One-day-old flies were immobilized by freezing at -80°C for imaging. These flies

were imaged using a BX53 microscope system with a MPLFLN 20x objective lens (Olympus, Tokyo, Japan). The phenotypic scores were calculated using Flynotyper.[22] Experimental analyses were performed using Prism 9 (GraphPad Software Inc., San Diego, CA, USA). The distribution of our data was determined using the D'Agostino & Pearson test and the Kolmogorov-Smirnov test (normality test was passed if $p > 0.05$). For data following a Gaussian distribution, we used ordinary one-way ANOVA with Tukey's multiple comparisons between groups.

Supplemental Figures

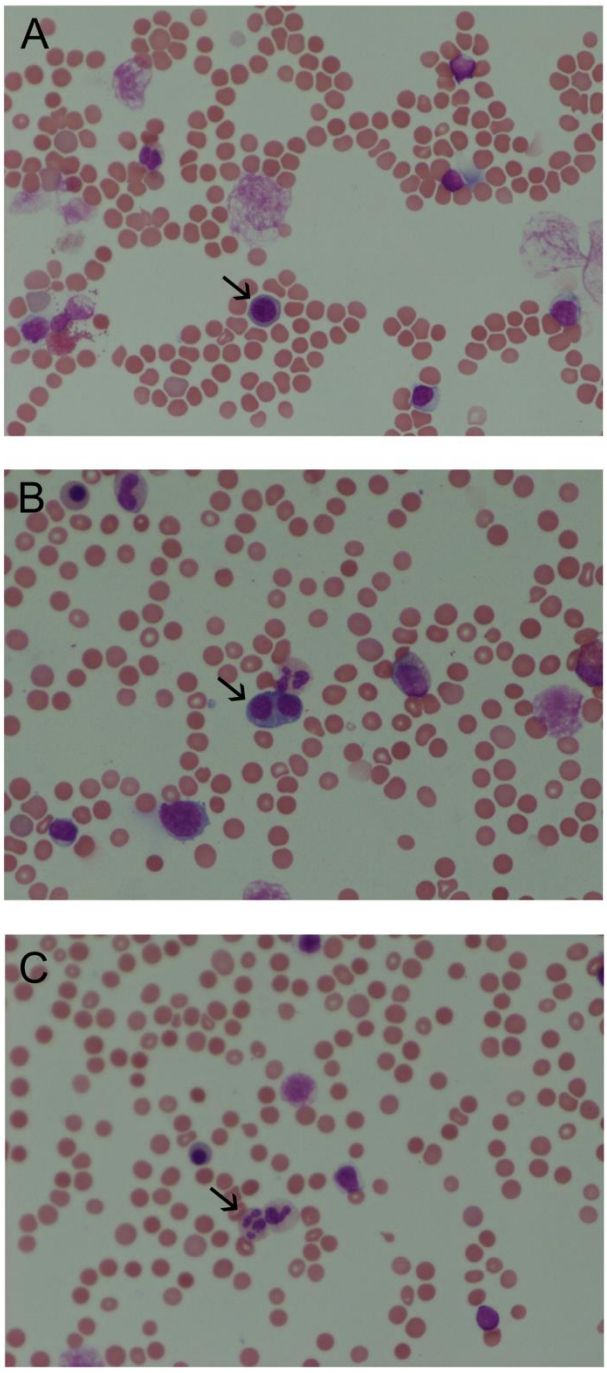

Figure S1 – Bone marrow aspirate smear from Individual 8

Bone-marrow examination in Individual 8 (age 8 years) revealed hypocellular marrow, signs of haemolysis, and evidence for haematopoiesis and myelodysplastic syndrome with aplastic anaemia. Arrows highlight examples of megaloblastic changes (A), binucleated erythroblasts (B), and Pseudo-Pelger–Huët anomalies (C) observed in the sample.

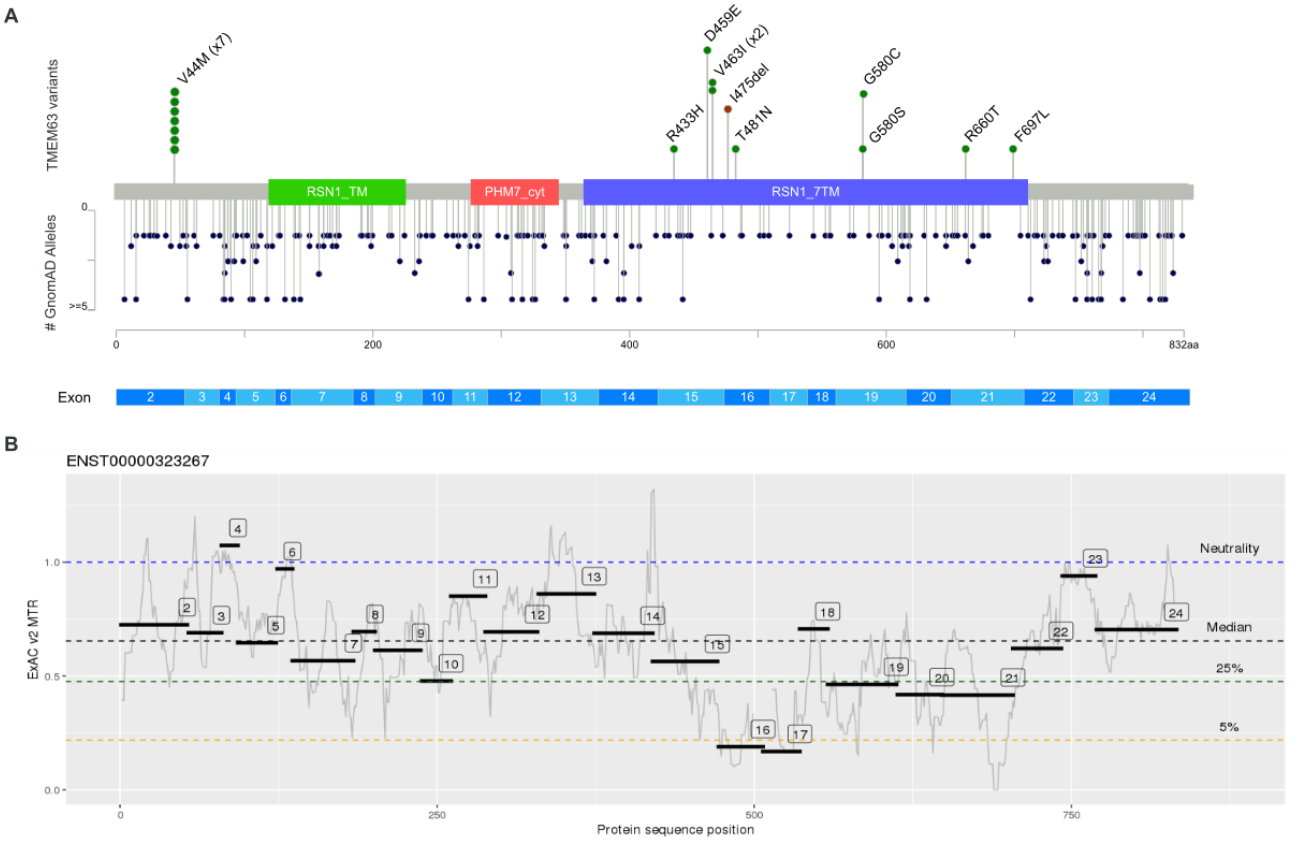

Figure S2 - Distribution of *TMEM63B* variants in our cohort and in reference population

(A) The lollipop diagram shows the distribution of the *TMEM63B* variants observed in our cohort (top, missense variants in green, in-frame deletion in brown) versus the reference population in GnomAD 2.1 (bottom, missense variants all in dark blue) on the linear protein map and relative to the Pfam-identified domains (RSN1_7TM, PF02714, green; PHM7_cyt, PF14703, red; RSN1_TM, PF13967, blue) of the protein and the *TMEM63B* exons (NM_018426.3, ENST00000323267). All but one of the *TMEM63B* variants in our cohort map in the RSN1_7TM domain (PF02714), which is conserved among osmosensitive calcium-permeable cation channels.[23] In the bottom panel, the length of the lollipop reflects the number of alleles in GnomAD 2.1 (see the Y-Axis on the left). The variants in our cohort maps in positions which are under constraint for missense variants. (B) The missense tolerance ratio (MTR)-Viewer tool[8] shows the local constraint with respect to the *TMEM63B* exons: all the variants in our cohort fall in regions where the MTR scores were below the neutrality threshold. The exon 16, bearing the T481N and the I475del variants, has the highest intolerance to missense substitutions, followed by the exons 15 (R433H, D459E, and V463I), 19 (G580S and G580C), 21 (R660T and F697L), and 2 (V44M).

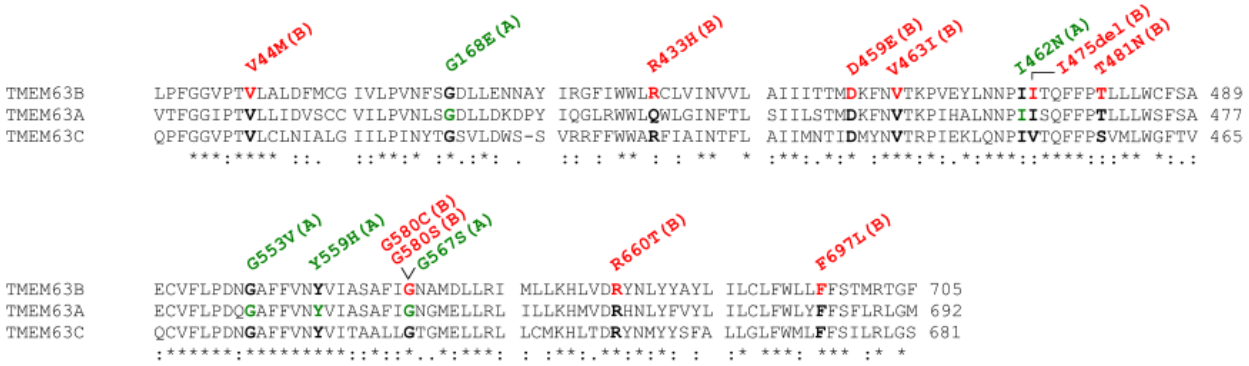

Figure S3 - Multiple sequence alignment of TMEM63A, B and C

The alignment shows the protein sequence of the human TMEM63B protein (NP_060896.1) and of its two paralogues TMEM63A (NP_055513.2) and TMEM63C (NP_065164.2). The residues affected by heterozygous variants of *TMEM63B* (our cohort, red) or *TMEM63A* (from the literature, green)[24–26] are in bold. The details of the variants are displayed above the alignments. The asterisk below the tracks indicates positions which have a single, fully conserved residue between all the input sequences, the colon indicates conservation between groups of strongly similar properties, and the period indicates conservation between groups of weakly similar properties. Six out ten *TMEM63B* variants in our cohort affected residues which are fully conserved among all the three paralogues' sequences (V44, D459, V463, G580, R660, and F697), and three affected residues conserved among two of the three paralogues and maintaining strongly similar properties in the other one (R443, T481 and I475).

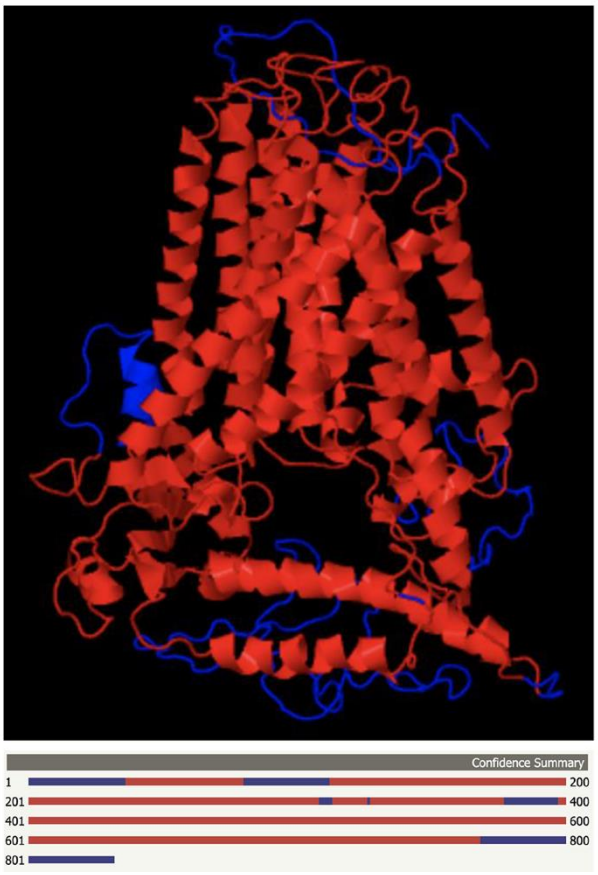

Figure S4 - Projection of confidence score for the TMEM63B protein structure

In the multi-template homology model obtained by Phyre2, the 81% of residues were modelled with >90% confidence and are showed in red both in the model (upper panel, side vision from the membrane plane) and in the confidence summary (lower panel, linear representation of the amino acids sequence), where low-confidence regions are in blue.

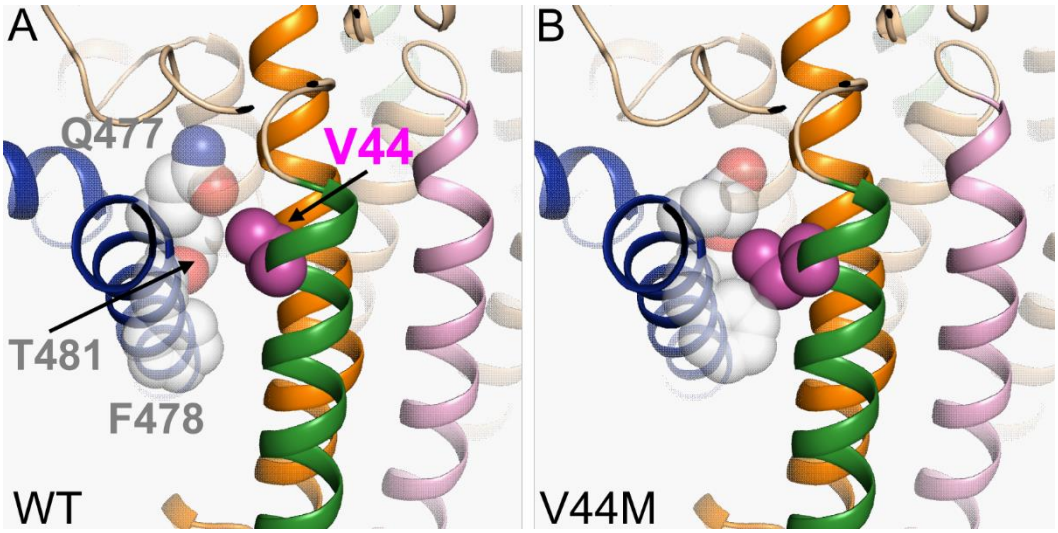

Figure S5 - Close-up of the protein region around Valine 44 in the WT and p.Val44Met TMEM63B

Transmembrane helices are colored as in Figure 3. V44 (purple) and the interacting residues G477, F478, and T481 are indicated by van der Waals spheres in the WT (A) and p.Val44Met mutated (B) model of the protein modeled by FoldX.

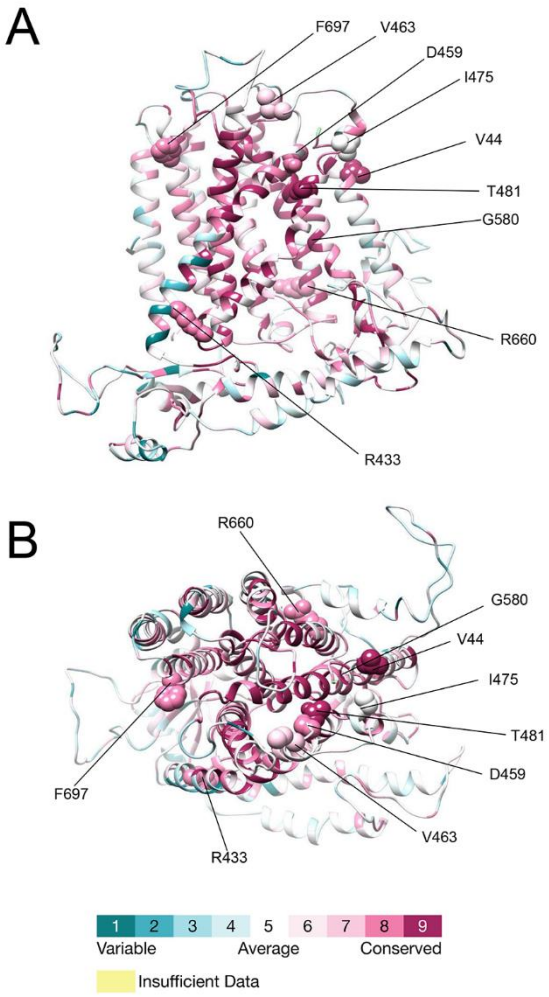

Figure S6 - ConSurf's projection of conservation scores onto the predicted structure of TMEM63B

View of the predicted structure of TMEM63B from the membrane plane (A) and the extracellular side (B). The color scale is dark aqua (least conserved) to dark magenta (most conserved). Detailed scored and prediction information for each of the residues affected by variants in our cohort are provided in Tables S2 and S3.

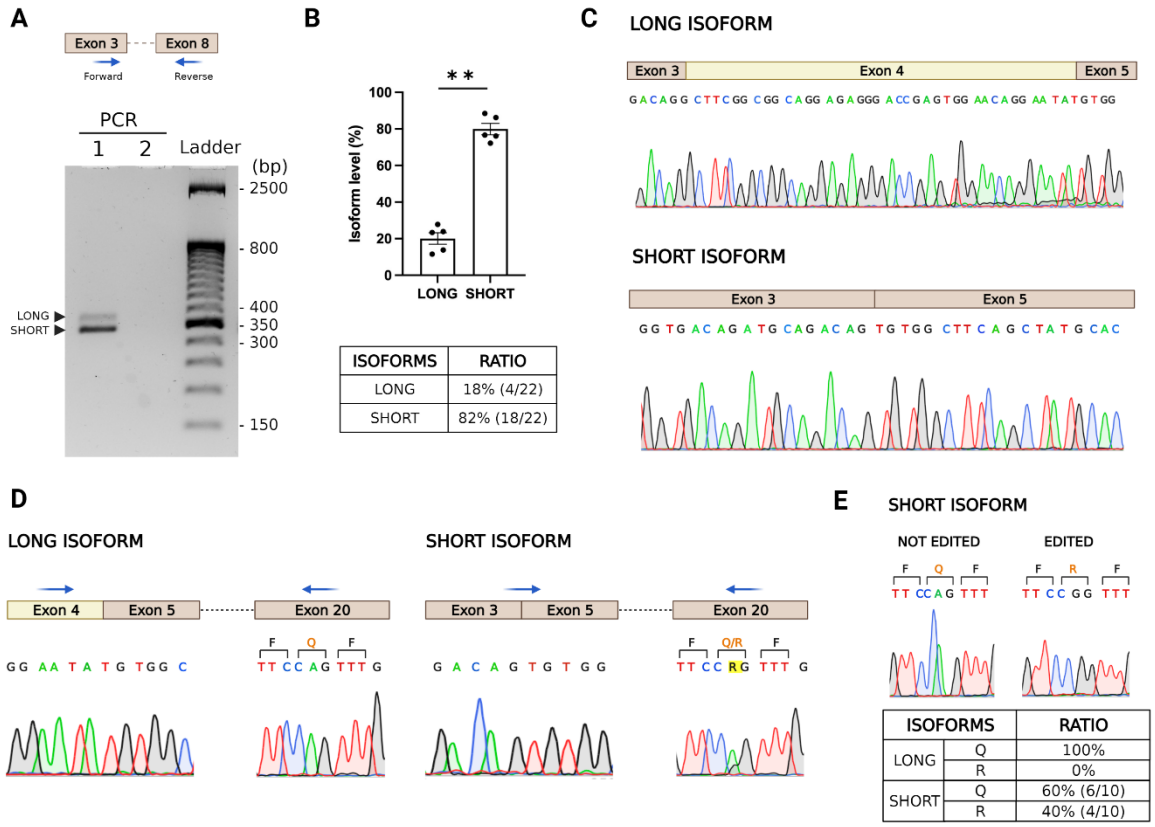

Figure S7 - Characterisation of alternative splicing of exon 4 and Q/R editing at exon 20 in *TMEM63B* RNA from human cerebral cortex

(A) Upper panel: schematic representation of *TMEM63B* exons 3-8 with arrows indicating Forward and Reverse primers for PCR amplification. Lower panel: agarose gel electrophoresis of the PCR products (Lane 1) showing both long and short *TMEM63B* isoforms, indicated by arrowheads. Lane 2, blank. (B) Upper panel: densitometric quantification of long and short isoforms from gel electrophoresis (data from 5 replicates, expressed as mean ± SEM. **p= 0.0079; Mann-Whitney U test). Lower panel: quantification of long and short isoforms levels obtained from TOPO TA cloning and subsequent sequencing of the PCR products expressed as the number of colonies containing the specific isoform over the total number of screened colonies. (C) Electropherograms from excised bands sequencing showing that exon 4 is only included in the long isoform. (D) Electropherograms of long and short isoforms showing exon 3-5 junctions and editing site at exon 20. A schematic representation of the corresponding exons is indicated, with blue arrows showing Forward and Reverse primers used for PCR amplification. For exon 20 the corresponding amino acids are reported above the nucleotide sequences at the editing site. (E) Upper panel: electropherograms of short edited and not edited isoforms showing the editing site at exon 20, obtained from TOPO TA cloning and subsequent sequencing of the short isoform PCR products. Lower panel: quantification of Q/R editing occurrence in long and short isoforms by TOPO TA technology. For each isoform, the percentage of editing occurrence is obtained from the ratio between the number of colonies edited (R) or not edited (Q) and the total number of analysed colonies.

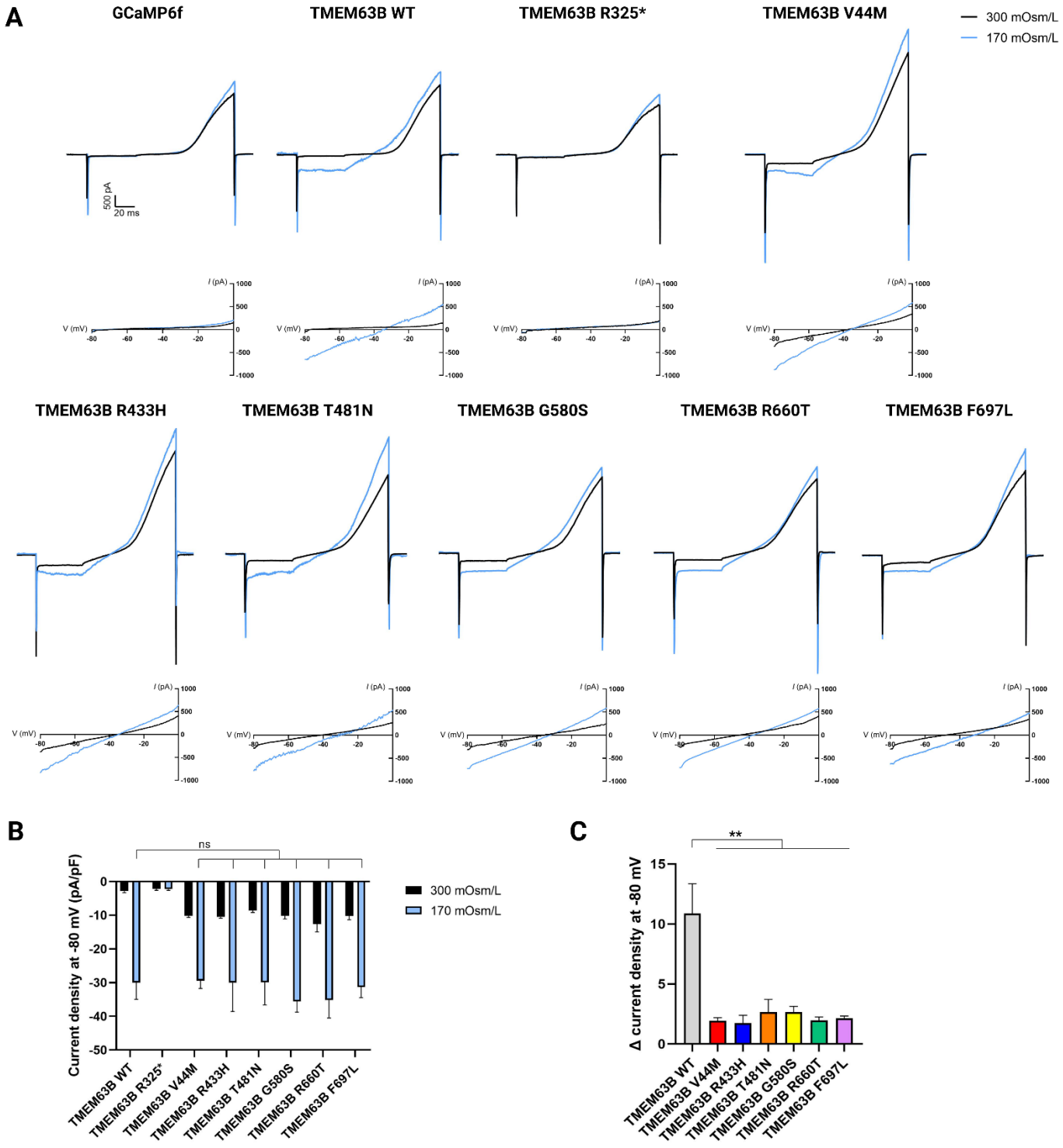

Figure S8 - Effect of hypo-osmotic stimulation on TMEM63B-mediated currents

(A) Representative current traces and current-voltage (I-V) relationships measured in Neuro2A cells transfected with GCaMP6f, TMEM63B WT or mutant plasmids and recorded with a -80 to + 80mV voltage ramp protocol in isotonic (300 mOsm/L) and hypo-osmotic (170 mOsm/L) conditions. (B) Quantification of whole-cell current density at -80 mV under isotonic and hypo-osmotic conditions (TMEM63B WT, R433H, T481N, G580S, and R660T = 6 cells, TMEM63B R325*, V44M, and F697L = 7 cells; ns = not significant,

Kruskal–Wallis and Dunn's multiple comparisons tests). (C) Quantification of the Δ current density measured at -80 mV between hypo-osmotic and isotonic conditions, calculated as:

$$\Delta \text{ current density at -80 mV} = \frac{(\text{hypo-osmotic current density}) - (\text{isotonic current density})}{(\text{isotonic current density})}$$

(TMEM63B WT, R433H, T481N, G580S, and R660T = 6 cells, TMEM63B V44M and F697L = 7 cells; **p<0.01, Kruskal–Wallis and Dunn's multiple comparisons tests). Data are expressed as mean ± SEM.

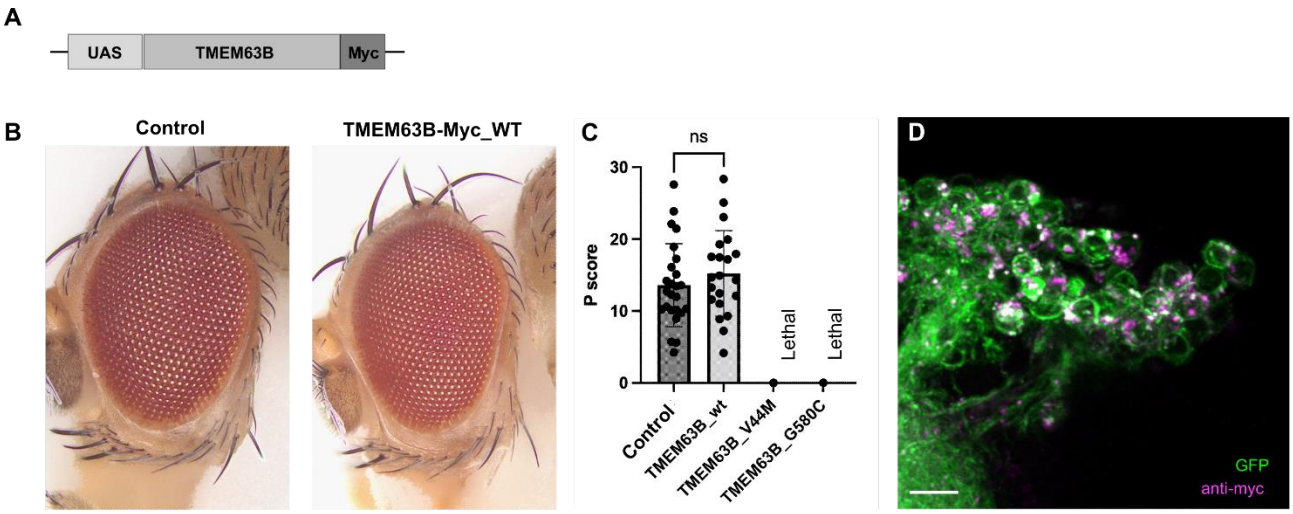

Figure S9 - Evaluation of human *TMEM63B* variants in *Drosophila*

(A) Cartoon depicting a *TMEM63B* gene construct with a Myc tag in UAS-based vector. (B) Representative bright-field microscope images of the eyes in control and WT TMEM63B-expressing flies (*GMR-Gal4* driver), and (C) quantification of the phenotypic scores in control ($n = 25$) and WT *TMEM63B* ($n = 21$), showing no significant differences in the eye morphology between the control and the WT *TMEM63B*-expressing flies. No data could be obtained for the V44M and G580C-expressing flies, as none of them reached the adult file stage. Data represent the mean ± SD (ns, not significant). (D) Three-dimensional projection of CD8:GFP-labeled Kenyon cells and myc-tagged WT TMEM63B in a posterior brain view in the adult stage. Scale bar = 10 μm.

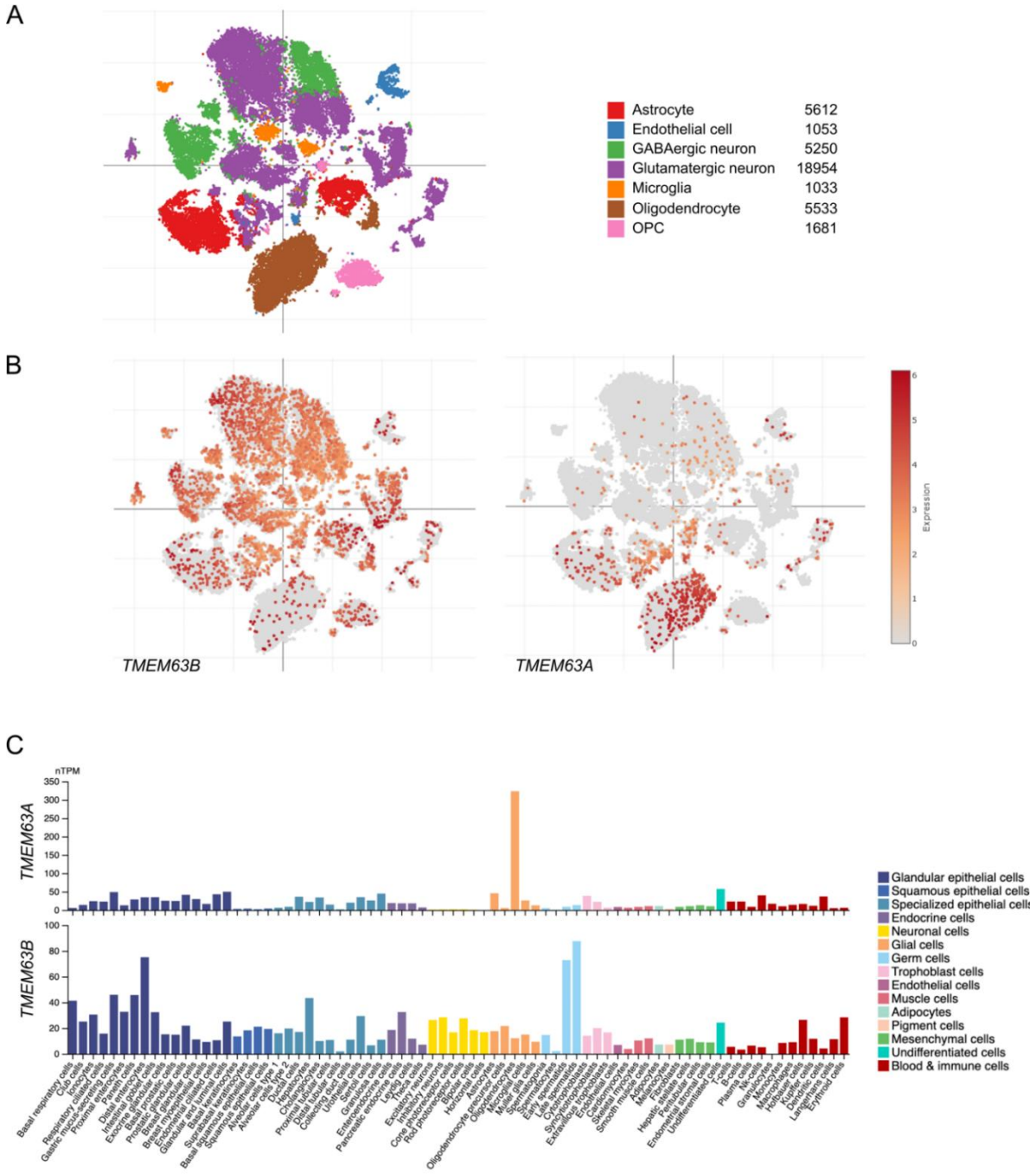

Figure S10 – Single-nucleus expression patterns of *TMEM63B* and *TMEM63A* in the human brain cortex

Panels A and B show the t-distributed stochastic neighbourhood embedding (tSNE) visualization of single-nucleus profiles (dots) coloured by cell type (A) and gene expression level (B). Single-nucleus RNA-seq data are shown according to the Single Cell Portal (https://singlecell.broadinstitute.org/single_cell/study/SCP381/).[27] (C) A summary of single cell RNA expression levels of *TMEM63A* and *B* as presented in the Human Protein Atlas (https://www.proteinatlas.org/). Color-coding is based on cell type groups (detailed on the right), each consisting of cell types with functional features in common. Abbreviations: pTPM, transcripts per million.

Supplemental Tables

Table S1 – Methods for exome/genome sequencing in the cohort.

Subject's ID	Sequencing approach, with reference
1-3	trio WES [28]
4	trio WGS [29,30]
5, 12	trio WES [31]
6	trio WGS [32]
7	singleton WES [33]
8, 15	trio WES [34]
9	trio WES [35]
10	singleton WES [36]
11	trio WES [37]
13	trio WES [38]
14	trio WES [39]
16	trio WES [40]
17	trio WES [41]

Table S2 - Auxological parameters and additional clinical and genetic findings of the 17 individuals with *TMEM63B* variants

Individual number/gender	***TMEM63B* variant (abbreviated form)**	**Weight, length, and head circumference (percentiles), at birth and subsequent follow-up**	**Hearing evaluation (age of formal test where available)**	**Additional clinical findings including haematological haematological manifestations**	**Additional genetic findings**
1/M	V44M	W 3-15th, L<3rd, HC 25-50th; 2y: W <3rd, L 50th, HC 25-50th	8y: normal BAEPS	6m: mild anaemia, mildly increased PLT count, stable on yearly FBC; OFT negative	No other clinically relevant variants
2/M	R433H	W 15-50th, L 15-50th, HC 15-50th; 10y: W <3rd, L >95th, HC 8th	10y: normal BAEPS and audiometric test	6y: high Hb level, 10y: mild abnormalities of RBC, MCV, MCH, no anaemia; OFT negative	No other clinically relevant variants
3/M	T481N	NA	2y: normal audiometric test	None	No other clinically relevant variants
4/M	V44M	W 91-98th, HC 91-98th; 9y: W 50th	4-5w: normal AOAE; no concerns from parents or professionals about individual's hearing (able to respond to auditory stimuli)	Jaundice at birth, then intermittent throughout life but less prominent. From 12m: macrocytic anaemia (leukoerythroblastic picture with nucleated red cells and myelocytes), borderline monocytosis, hepatosplenomegaly. 5y: cholecystectomy for chronic cholecystitis, liver biopsy showed haemosiderin deposits. From 7y: persistent macrocytic anaemia with reticulocytosis, increased stomatocytes, iron deficiency anaemia. From 8y: recurrent chest infections. 10y: RCMO onset (flare-up of osteomyelitis associated with Hb reduction and alopecia patches). From age 10y: transfusion dependent (monthly), severe anaemia, BM: increased RBC production (due to haemolysis), EMA binding test normal, blood film suggested hereditary elliptocytosis, negative genetic test for hereditary spherocytosis	No other clinically relevant variants
5/M	V44M	W 25-50th; 5y: HC 10th; 7y: W 1st, L 30th	No clinical concerns of hearing impairment; no formal hearing test	Jaundice at birth; laryngomalacia (supraglottoplasty at 1y)	No other clinically relevant variants
6/F	V44M	W >99th; 14m: W >99th, L >99th	No clinical concerns of hearing impairment; no formal hearing test	From birth: unexplained macrocytic anaemia, EMA-test analysis normal, haemoglobinopathy screen normal, haemolysis screen negative, negative red cell anaemia TGP, mild hepatosplenomegaly, required transfusion. From 4m to 7m: jaundice. Pharyngomalacia and severe OSA leading to respiratory failure and NIV requirement, recurrent chest infections	No other clinically relevant variants

7/M	V44M	W 60th, L 44th, HC 35th; 20m: W 75th, L >90th, HC 25-50th	3w: normal AOAE	From 12m: scleralicterus	No other clinically relevant variants
8/F	V44M	W 15-50th, L 85-97th, HC 50-85th; 17y: W<5th, L<5th	7 and 10y: normal BAEPs	From 2y: severe anaemia, occasional transfusions, episode of haemolysis triggered by infection. 8y BM showed myelodysplastic syndrome with aplastic anaemia, haematopoiesis, and chronic haemolysis	No other clinically relevant variants
9/M	V44M	W 50th, L 60th, HC 35th; 1y: HC <5th; 10y W 60th; 15y: W <5th, HC <5th	No clinical concerns of hearing impairment; no formal hearing test	Mild and stable anaemia noticed since age 2y (no previous measurement available); retinal dystrophy	*de novo CBL* NM_005188.3:c.1110A>C p.(Leu370Phe); classified as VUS with uncertain contribute to the phenotype (developmental delay)
10/F	D459E	W 62nd, L<3rd HC 83rd; 3y: W 45th, L 73rd, HC 10-25th	No formal hearing test performed, but clinical concern for poor hearing	Fraternal twin, preterm labor, pre-eclampsia, gestational diabetes, pulmonary valve stenosis, hyperbilirubinemia, 2.5y: mild macrocytic anaemia; OFT negative	No other clinically relevant variants
11/M	V463I	W 25-50th; L 25-50th; HC 50-75th; 4y: W 31st, L 23rd; HC 33rd	No clinical concerns of hearing impairment; no formal hearing test	None	No other clinically relevant variants
12/M	V463I	W 25-50th; L 76th; HC 20th; 2y: W 75th; L 59th; HC >99th (+3.43 SD)	1w: normal AOAE	None	*de novo TSC1* NM_000368.5:c.1498C>T p.(Arg500*); described by van Slegtenhorst et al 1999[42]; classified as pathogenic and thought to contribute to the phenotype (macrocephaly)
13/F	I475del	W 3-5th, L 25-50th, HC <3rd; 12y: HC <5th; 16y: W <5th, L<5th	9m: normal BAEPs	From birth, severe haemolytic anaemia with macrocytosis, thrombocytopenia and hepatosplenomegaly, transfusion dependent, hyperbilirubinemia (total bilirubin 37 µmol/l, direct bilirubin 7 µmol/l), left vesicoureteral reflux (surgical correction 13y), chronic urinary retention	No other clinically relevant variants
14/M	G580S	W 50th, L 50th, HC 50th; 4.5y: W <3rd, L<3rd, HC<3rd	No clinical concerns of hearing impairment; no formal hearing test	None	No other clinically relevant variants
15/F	G580C	W 15-50th, L <3rd, HC 15-50th; 15y: W 5-10th, L <5th, HC 50-75th	27y: abnormal BAEPs (left ear: disappearance of II to V waves; right ear: disappearance of II to IV waves and latency prolongation of V wave).	Slight bilirubin increase	No other clinically relevant variants

16/F	R660T	W 50-75th, L 90-95th; 23m: W >97th, L 50-75th, HC >97th	Failed newborn AOAE on the left ear; clinical concern for mid hearing loss; 1y, 11m: AOAE inconclusive; tympanometric tests showed normal middle ear function bilaterally	Birth: mild jaundice, macrocytic anaemia, out-turned feet	arr[GRCh38/hg38] 20p13(391190_508758)x3; classified as VOUS
17/M	F697L	W<3rd; 15y W<3rd, L<3rd	9y: normal audiometric test	None	Maternally inherited *GCK* NM_000162.5:c.107G>A p.(Arg36Gln); described by Osbak et al, 2009[43] - risk factor for type 2 diabetes, reported as unsolicited finding[#]

Additional genetic findings, where reported, were classified according to the ACMG guidelines.[44,45] A comment is provided to illustrate whether the variants is thought to have contributed to the observed phenotype. Abbreviations and symbols: AOAE, automated otoacoustic emission test; BAEPs, brainstem auditory evoked potentials; BM, bone marrow; RCMO, recurrent chronic multifocal osteomyelitis; EMA, eosin-5′-maleimide-binding; F, female; FBC, full blood count; Hb, haemoglobin; HC, head circumference; L, length; M, male; m, months; MCH, mean corpuscular haemoglobin; MCV, mean corpuscular volume; m, months; NA, not available/not applicable; NIV, non-invasive ventilation; OFT, osmotic fragility test; OSA, obstructive sleep apnoea; PLT, platelets; RBC, red blood cells; TGP, targeted gene panel; VUS, variant of uncertain significance; W, weight; w, weeks; y, years; [#]No family members with type 2 diabetes at the time of WES; increased glucose levels in the mother during the pregnancy.

Table S3 - Genomic coordinates and in-silico analysis of the *TMEM63B* variants in our cohort

ID	Variant (genomic GRCh37/hg19)	Protein Change	Exon	GnomAD (v2.1)	TOPMed (Freeze 8)	CADD	SIFT/score	Polyphen-2/score	MutationTaster/score	PhyloP100way	GERP++	Grantham score	Tolerance Score (dN/dS, Metadome)
1, 4-9	6:g.44102451G>A	V44M	2	.	.	26.6	deleterious/0	probably_damaging/0.999	disease_causing/0.99	9.23	4.23	21	0.42
2	6:g.44116567G>A	R433H	15	.	.	29.1	deleterious/0	probably_damaging/0.934	disease_causing/0.99	7.73	4.23	29	0.31
3	6:g.44117624C>A	T481N	16	.	.	25.7	deleterious/0	probably_damaging/0.992	disease_causing/1	7.59	4.48	65	0.08
10	6:g.44116646C>G	D459E	15	.	.	24.5	deleterious/0	probably_damaging/0.943	disease_causing/0.99	3.86	4.48	45	0.15
11-12	6:g.44116656G>A	V463I	15	.	.	26.5	deleterious/0	possibly_damaging/0.85	disease_causing/0.99	9.52	4.48	29	0.16
13	6:g.44117600CCAT>C	I475del	16	.	.	NA	NA	NA	disease_causing/1	7.31	4.48	NA	0.11
14	6:g.44119647G>A	G580S	19	.	.	31	deleterious/0	probably_damaging/0.999	disease_causing/1	9.58	5.01	56	0.14
15	6:g.44119647G>T	G580C	19	.	.	32	deleterious/0	probably_damaging/1	disease_causing/1	10	5.01	159	0.14
16	6:g.44121449G>C	R660T	21	.	.	26.6	deleterious/0	probably_damaging/0.955	disease_causing/0.99	9.26	4.59	71	0.31
17	6:g.44121559T>C	F697L	21	.	.	30	deleterious/0	probably_damaging/0.968	disease_causing/0.99	7.52	4.62	22	0.06

The table shows the coordinates of the variants according to the recommendations of the Human Genome Variation Society (http://varnomen.hgvs.org/), based on the hGRCh37/hg19 assembly and the NM_018426.3 reference transcript. None of the variants was reported in publicly available allele frequency databases such as GnomAD (v2.1) and TOPMed (Freeze 8). For all the variants in our cohort we report the *in-silico* predictions of pathogenicity obtained from multiple tools: for CADD (Combined Annotation-

Dependent Depletion) the PHRED-like scaled C-score greater or equal 20 indicates the 1% most deleterious substitutions to the gene products;[46] SIFT confidence score for a missense variant is computed as 1-p where p is the probability for the variant to be deleterious [47]; for MutationTaster a value close to 1 indicates a high 'security' of the prediction, while for Polyphen-2 it represents the probability for the variant to be disease causing in a 0-1 range) [48]. PhyloP100way and GERP++ scores range from -14.1 to 6.4 and -12.3 to 6.17 respectively, with higher scores indicating stronger constraint.[5,6] Grantham score ranges from 5 to 215 and predicts the distance between two amino acids, in an evolutionary sense. Higher Grantham scores are considered more deleterious.[49] Tolerance Scores (dN/dS nonsynonymous over synonymous ratio according to Metadome) range from highly intolerant (0-0.19) to intolerant (0.2-0.49).[7] NA: not available/not applicable.

Table S4 – Structural analysis of the *TMEM63B* variants by Consurf and Missense3D

ID	Protein Change	Transmembrane domain	Protein domain (Pfam 35.0)	ConSurf scale/prediction	Missense3D prediction
1, 4-9	V44M	TM1	NA	9/predicted structural residue (highly conserved and buried)	Expansion of cavity volume by 8.208 Å^3
2	R433H	TM4	PF02714	8/buried residue	Contraction of cavity volume by 3.888 Å^3
3	T481N	TM5	PF02714	9/predicted structural residue (highly conserved and buried)	No structural damage detected; Unable to calculate cavity in mutant structure
10	D459E	TM4	PF02714	8/predicted functional residue (highly conserved and exposed)	Buried salt bridge breakage (Asp 459, LYS 460)
11, 12	V463I	TM4	PF02714	8/buried residue	Contraction of cavity volume by 13.824 Å^3
13	I475del	TM5	PF02714	5/buried residue	NA
14	G580S	TM7	PF02714	9/predicted structural residue (highly conserved and buried)	Buried Gly residue (RSA 5.9%) replaced with a buried Ser residue (RSA 3.8%); Contraction of cavity volume by 52.056 Å^3
15	G580C	TM7	PF02714	9/predicted structural residue (highly conserved and buried)	Buried Gly residue (RSA 5.9%) replaced with a buried Cys residue (RSA 3.7%); Contraction of cavity volume by 66.744 Å^3
16	R660T	TM8	PF02714	8/predicted functional residue (highly conserved and exposed)	Buried charge replaced (Arg, RSA 5.6%) with an uncharged residue (Thr); Buried salt bridge breakage (Arg 660, Asp 137); Expansion of cavity volume by 60.696 Å^3
17	F697L	TM9	PF02714	8/buried residue	Expansion of cavity volume by 30.24 Å^3

All the affected residues map in a transmembrane (TM) domain, and all but the recurrent V44M are in the RSN1_7TM (PF02714) domain.[50] For all the affected residues, we report the conservation scale (ranging from variable, 1 to conserved, 9) and the neural-network algorithm prediction from ConSurf (https://consurf.tau.ac.il/).[15] For all missense variants, we also show the prediction of possible structural changes according to Missense3D-DB, which considered 17 structural features, including secondary structure alterations, non-covalent bond breakages, and buried residues changes.[16] NA: not available/not applicable.

Supplemental References

1. Li, H., and Durbin, R. (2009). Fast and accurate short read alignment with Burrows-Wheeler transform. Bioinformatics *25*, 1754–1760. 10.1093/bioinformatics/btp324.
2. DePristo, M.A., Banks, E., Poplin, R., Garimella, K. V., Maguire, J.R., Hartl, C., Philippakis, A.A., del Angel, G., Rivas, M.A., Hanna, M., et al. (2011). A framework for variation discovery and genotyping using next-generation DNA sequencing data. Nat. Genet. *43*, 491–498. 10.1038/ng.806.
3. Lek, M., Karczewski, K.J., Minikel, E. V., Samocha, K.E., Banks, E., Fennell, T., O'Donnell-Luria, A.H., Ware, J.S., Hill, A.J., Cummings, B.B., et al. (2016). Analysis of protein-coding genetic variation in 60,706 humans. Nature. 10.1038/nature19057.
4. Liu, X., Jian, X., and Boerwinkle, E. (2011). dbNSFP: a lightweight database of human nonsynonymous SNPs and their functional predictions. Hum. Mutat. *32*, 894–899. 10.1002/humu.21517.
5. Cooper, G.M., Stone, E.A., Asimenos, G., Green, E.D., Batzoglou, S., and Sidow, A. (2005). Distribution and intensity of constraint in mammalian genomic sequence. Genome Res. *15*, 901–913. 10.1101/gr.3577405.
6. Pollard, K.S., Hubisz, M.J., Rosenbloom, K.R., and Siepel, A. (2010). Detection of nonneutral substitution rates on mammalian phylogenies. Genome Res. *20*, 110–121. 10.1101/gr.097857.109.
7. Wiel, L., Baakman, C., Gilissen, D., Veltman, J.A., Vriend, G., and Gilissen, C. (2019). MetaDome: Pathogenicity analysis of genetic variants through aggregation of homologous human protein domains. Hum. Mutat. *40*, humu.23798. 10.1002/humu.23798.
8. Traynelis, J., Silk, M., Wang, Q., Berkovic, S.F., Liu, L., Ascher, D.B., Balding, D.J., and Petrovski, S. (2017). Optimizing genomic medicine in epilepsy through a gene-customized approach to missense variant interpretation. Genome Res. *27*, 1715–1729. 10.1101/gr.226589.117.
9. Sayers, E.W., Bolton, E.E., Brister, J.R., Canese, K., Chan, J., Comeau, D.C., Connor, R., Funk, K., Kelly, C., Kim, S., et al. (2022). Database resources of the national center for biotechnology information. Nucleic Acids Res. *50*. 10.1093/nar/gkab1112.
10. Sievers, F., Wilm, A., Dineen, D., Gibson, T.J., Karplus, K., Li, W., Lopez, R., McWilliam, H., Remmert, M., Söding, J., et al. (2011). Fast, scalable generation of high-quality protein multiple

sequence alignments using Clustal Omega. Mol. Syst. Biol. *7*. 10.1038/msb.2011.75.

11. Kelley, L.A., Mezulis, S., Yates, C.M., Wass, M.N., and Sternberg, M.J.E. (2015). The Phyre2 web portal for protein modeling, prediction and analysis. Nat. Protoc. *10*. 10.1038/nprot.2015.053.

12. Schymkowitz, J., Borg, J., Stricher, F., Nys, R., Rousseau, F., and Serrano, L. (2005). The FoldX web server: An online force field. Nucleic Acids Res. *33*. 10.1093/nar/gki387.

13. Guerois, R., Nielsen, J.E., and Serrano, L. (2002). Predicting changes in the stability of proteins and protein complexes: A study of more than 1000 mutations. J. Mol. Biol. *320*. 10.1016/S0022-2836(02)00442-4.

14. Jumper, J., Evans, R., Pritzel, A., Green, T., Figurnov, M., Ronneberger, O., Tunyasuvunakool, K., Bates, R., Žídek, A., Potapenko, A., et al. (2021). Highly accurate protein structure prediction with AlphaFold. Nature *596*. 10.1038/s41586-021-03819-2.

15. Meier, A., and Söding, J. (2015). Automatic Prediction of Protein 3D Structures by Probabilistic Multi-template Homology Modeling. PLoS Comput. Biol. *11*. 10.1371/journal.pcbi.1004343.

16. Ittisoponpisan, S., Islam, S.A., Khanna, T., Alhuzimi, E., David, A., and Sternberg, M.J.E. (2019). Can Predicted Protein 3D Structures Provide Reliable Insights into whether Missense Variants Are Disease Associated? J. Mol. Biol. *431*. 10.1016/j.jmb.2019.04.009.

17. Pettersen, E.F., Goddard, T.D., Huang, C.C., Couch, G.S., Greenblatt, D.M., Meng, E.C., and Ferrin, T.E. (2004). UCSF Chimera - A visualization system for exploratory research and analysis. J. Comput. Chem. *25*. 10.1002/jcc.20084.

18. Du, H., Ye, C., Wu, D., Zang, Y.Y., Zhang, L., Chen, C., He, X.Y., Yang, J.J., Hu, P., Xu, Z., et al. (2020). The Cation Channel TMEM63B Is an Osmosensor Required for Hearing. Cell Rep. *31*. 10.1016/j.celrep.2020.107596.

19. Sugie, A., Möhl, C., Hakeda-Suzuki, S., Matsui, H., Suzuki, T., and Tavosanis, G. (2017). Analyzing synaptic modulation of drosophila melanogaster photoreceptors after exposure to prolonged light. J. Vis. Exp. *2017*. 10.3791/55176.

20. Groth, A.C., Fish, M., Nusse, R., and Calos, M.P. (2004). Construction of transgenic Drosophila by using the site-specific integrase from phage phiC31. Genetics *166*, 1775–1782. 10.1534/genetics.166.4.1775.

21. Kramer, J.M., and Staveley, B.E. (2003). GAL4 causes developmental defects and apoptosis when expressed in the developing eye of Drosophila melanogaster. Genet. Mol. Res. *2*.

22. Iyer, J., Wang, Q., Le, T., Pizzo, L., Grönke, S., Ambegaokar, S.S., Imai, Y., Srivastava, A., Troisí, B.L., Mardon, G., et al. (2016). Quantitative Assessment of Eye Phenotypes for Functional Genetic Studies Using *Drosophila melanogaster*. G3 Genes|Genomes|Genetics *6*, 1427–1437. 10.1534/g3.116.027060.

23. Hou, C., Tian, W., Kleist, T., He, K., Garcia, V., Bai, F., Hao, Y., Luan, S., and Li, L. (2014). DUF221 proteins are a family of osmosensitive calcium-permeable cation channels conserved across eukaryotes. Cell Res. *24*. 10.1038/cr.2014.14.

24. Yan, H., Helman, G., Murthy, S.E., Ji, H., Crawford, J., Kubisiak, T., Bent, S.J., Xiao, J., Taft, R.J., Coombs, A., et al. (2019). Heterozygous Variants in the Mechanosensitive Ion Channel TMEM63A Result in Transient Hypomyelination during Infancy. Am. J. Hum. Genet. *105*, 996–1004. 10.1016/j.ajhg.2019.09.011.

25. Tonduti, D., Mura, E., Masnada, S., Bertini, E., Aiello, C., Zini, D., Parmeggiani, L., Cantalupo, G., Talenti, G., Veggiotti, P., et al. (2021). Spinal cord involvement and paroxysmal events in "Infantile Onset Transient Hypomyelination" due to TMEM63A mutation. J. Hum. Genet. *66*, 1035–1037. 10.1038/s10038-021-00921-1.

26. Fukumura, S., Hiraide, T., Yamamoto, A., Tsuchida, K., Aoto, K., Nakashima, M., and Saitsu, H. (2022). A novel de novo TMEM63A variant in a patient with severe hypomyelination and global developmental delay. Brain Dev. *44*, 178–183. 10.1016/j.braindev.2021.09.006.

27. Gaublomme, J.T., Li, B., McCabe, C., Knecht, A., Yang, Y., Drokhlyansky, E., Van Wittenberghe, N., Waldman, J., Dionne, D., Nguyen, L., et al. (2019). Nuclei multiplexing with barcoded antibodies for single-nucleus genomics. Nat. Commun. *10*. 10.1038/s41467-019-10756-2.

28. Vetro, A., Nielsen, H.N., Holm, R., Hevner, R.F., Parrini, E., Powis, Z., Møller, R.S., Bellan, C., Simonati, A., Lesca, G., et al. (2021). ATP1A2-and ATP1A3-associated early profound epileptic encephalopathy and polymicrogyria. Brain *144*. 10.1093/brain/awab052.

29. Wright, C.F., Fitzgerald, T.W., Jones, W.D., Clayton, S., McRae, J.F., Van Kogelenberg, M., King, D.A., Ambridge, K., Barrett, D.M., Bayzetinova, T., et al. (2015). Genetic diagnosis of developmental

disorders in the DDD study: A scalable analysis of genome-wide research data. Lancet *385*. 10.1016/S0140-6736(14)61705-0.

30. Fitzgerald, T.W., Gerety, S.S., Jones, W.D., Van Kogelenberg, M., King, D.A., McRae, J., Morley, K.I., Parthiban, V., Al-Turki, S., Ambridge, K., et al. (2015). Large-scale discovery of novel genetic causes of developmental disorders. Nature *519*. 10.1038/nature14135.

31. Dias, K.-R., Carlston, C.M., Blok, L.E.R., De Hayr, L., Nawaz, U., Evans, C.-A., Bayrak-Toydemir, P., Htun, S., Zhu, Y., Ma, A., et al. (2022). De Novo ZMYND8 variants result in an autosomal dominant neurodevelopmental disorder with cardiac malformations. Genet. Med. *24*, 1952–1966. 10.1016/j.gim.2022.06.001.

32. Genomes-Project-Pilot-Investigators, T. (2022). 100,000 genomes pilot on rare-disease diagnosis in health care – preliminary report. Yearb. Paediatr. Endocrinol. 10.1530/ey.19.15.16.

33. Brunet, T., Jech, R., Brugger, M., Kovacs, R., Alhaddad, B., Leszinski, G., Riedhammer, K.M., Westphal, D.S., Mahle, I., Mayerhanser, K., et al. (2021). De novo variants in neurodevelopmental disorders—experiences from a tertiary care center. Clin. Genet. *100*. 10.1111/cge.13946.

34. Sakamoto, M., Iwama, K., Sekiguchi, F., Mashimo, H., Kumada, S., Ishigaki, K., Okamoto, N., Behnam, M., Ghadami, M., Koshimizu, E., et al. (2021). Novel EXOSC9 variants cause pontocerebellar hypoplasia type 1D with spinal motor neuronopathy and cerebellar atrophy. J. Hum. Genet. *66*. 10.1038/s10038-020-00853-2.

35. Terhal, P.A., Vlaar, J.M., Middelkamp, S., Nievelstein, R.A.J., Nikkels, P.G.J., Ross, J., Créton, M., Bos, J.W., Voskuil-Kerkhof, E.S.M., Cuppen, E., et al. (2020). Biallelic variants in POLR3GL cause endosteal hyperostosis and oligodontia. Eur. J. Hum. Genet. *28*. 10.1038/s41431-019-0427-0.

36. Retterer, K., Juusola, J., Cho, M.T., Vitazka, P., Millan, F., Gibellini, F., Vertino-Bell, A., Smaoui, N., Neidich, J., Monaghan, K.G., et al. (2016). Clinical application of whole-exome sequencing across clinical indications. Genet. Med. *18*, 696–704. 10.1038/gim.2015.148.

37. Giacomini, T., Scala, M., Nobile, G., Severino, M., Tortora, D., Nobili, L., Accogli, A., Torella, A., Capra, V., Mancardi, M.M., et al. (2022). De novo POLR2A p.(Ile457Thr) variant associated with early-onset encephalopathy and cerebellar atrophy: expanding the phenotypic spectrum. Brain Dev. *44*, 480–485. 10.1016/j.braindev.2022.04.002.

38. Bergant, G., Maver, A., Lovrecic, L., Čuturilo, G., Hodzic, A., and Peterlin, B. (2018). Comprehensive use of extended exome analysis improves diagnostic yield in rare disease: A retrospective survey in 1,059 cases. Genet. Med. *20*, 303–312. 10.1038/gim.2017.142.

39. Larcher, L., Norris, J.W., Lejeune, E., Buratti, J., Mignot, C., Garel, C., Keren, B., Schwartz, C.E., and Whalen, S. (2020). The complete loss of function of the SMS gene results in a severe form of Snyder-Robinson syndrome. Eur. J. Med. Genet. *63*. 10.1016/j.ejmg.2019.103777.

40. Satterstrom, F.K., Kosmicki, J.A., Wang, J., Breen, M.S., De Rubeis, S., An, J.Y., Peng, M., Collins, R., Grove, J., Klei, L., et al. (2020). Large-Scale Exome Sequencing Study Implicates Both Developmental and Functional Changes in the Neurobiology of Autism. Cell *180*. 10.1016/j.cell.2019.12.036.

41. de Koning, M.A., Hoffer, M.J.V., Nibbeling, E.A.R., Bijlsma, E.K., Toirkens, M.J.P., Adama-Scheltema, P.N., Verweij, E.J., Veenhof, M.B., Santen, G.W.E., and Peeters-Scholte, C.M.P.C.D. (2022). Prenatal exome sequencing: A useful tool for the fetal neurologist. Clin. Genet. *101*. 10.1111/cge.14070.

42. Van Slegtenhorst, M., Verhoef, S., Tempelaars, A., Bakker, L., Wang, Q., Wessels, M., Bakker, R., Nellist, M., Lindhout, D., Halley, D., et al. (1999). Mutational spectrum of the TSC1 gene in a cohort of 225 tuberous sclerosis complex patients: No evidence for genotype-phenotype correlation. J. Med. Genet. *36*. 10.1136/jmg.36.4.285.

43. Osbak, K.K., Colclough, K., Saint-Martin, C., Beer, N.L., Bellanné-Chantelot, C., Ellard, S., and Gloyn, A.L. (2009). Update on mutations in glucokinase (GCK), which cause maturity-onset diabetes of the young, permanent neonatal diabetes, and hyperinsulinemic hypoglycemia. Hum. Mutat. *30*. 10.1002/humu.21110.

44. Richards, S., Aziz, N., Bale, S., Bick, D., Das, S., Gastier-Foster, J., Grody, W.W., Hegde, M., Lyon, E., Spector, E., et al. (2015). Standards and guidelines for the interpretation of sequence variants: A joint consensus recommendation of the American College of Medical Genetics and Genomics and the Association for Molecular Pathology. Genet. Med. *17*. 10.1038/gim.2015.30.

45. Riggs, E.R., Andersen, E.F., Cherry, A.M., Kantarci, S., Kearney, H., Patel, A., Raca, G., Ritter, D.I., South, S.T., Thorland, E.C., et al. (2020). Technical standards for the interpretation and reporting of

constitutional copy-number variants: a joint consensus recommendation of the American College of Medical Genetics and Genomics (ACMG) and the Clinical Genome Resource (ClinGen). Genet. Med. *22*. 10.1038/s41436-019-0686-8.

46. Rentzsch, P., Witten, D., Cooper, G.M., Shendure, J., and Kircher, M. (2019). CADD: predicting the deleteriousness of variants throughout the human genome. Nucleic Acids Res. *47*, D886–D894. 10.1093/nar/gky1016.

47. Kumar, P., Henikoff, S., and Ng, P.C. (2009). Predicting the effects of coding non-synonymous variants on protein function using the SIFT algorithm. Nat. Protoc. *4*, 1073–1081. 10.1038/nprot.2009.86.

48. Adzhubei, I.A., Schmidt, S., Peshkin, L., Ramensky, V.E., Gerasimova, A., Bork, P., Kondrashov, A.S., and Sunyaev, S.R. (2010). A method and server for predicting damaging missense mutations. Nat. Methods *7*, 248–249. 10.1038/nmeth0410-248.

49. Grantham, R. (1974). Amino acid difference formula to help explain protein evolution. Science (80-.). *185*. 10.1126/science.185.4154.862.

50. Mistry, J., Chuguransky, S., Williams, L., Qureshi, M., Salazar, G.A., Sonnhammer, E.L.L., Tosatto, S.C.E., Paladin, L., Raj, S., Richardson, L.J., et al. (2021). Pfam: The protein families database in 2021. Nucleic Acids Res. *49*. 10.1093/nar/gkaa913.